TABLE 1. SEQUENCE VARIANTS IN THE TWO FAMILIES FOUND BY WHOLE-EXOME SEQUENCING

	Family A		Family B	
	NextGENe	MAQ	NextGENe	MAQ
Total variant calls	118,801	170,093	130,791	175,155
Unknown SNP variants (dbSNP132, 1000 Genomes project)	28,620	22,038	34,627	21,687
SNVs commonly found by two methods	3,269		2,347	
NS+SP (indels)[a]	671	(100)	454	(135)
Present among 45 candidate genes	1		1	
Confirmed segregation (heterozygous)	1		1	

[a]Small indels were detected only by NextGENe. SNP, single nucleotide polymorphism; SNV, single nucleotide variant; NS, non-synonymous variants; SP, canonical splice site variants; indels, small insertions or deletions.

DISCUSSION

In this study, a pathogenic mutation in *CRYAA* or *CRYGC*, which encode a crystallin family protein, was identified in each of two Korean families with congenital cataract. Crystallin constitutes the major protein of the vertebrate eye lens and is classified into three main types: α-, β-, and γ-crystallin. *CRYAA*, encoding αA-crystallin, maps to chromosome 21q22.3, and mutations have been reported in autosomal dominant congenital cataract [13]. The αA-crystallin protein consists of an N-terminal region, a conserved α-crystallin domain, and a short C-terminal region. The α-crystallin domain may be involved in aggregating and disaggregating larger protein complexes, whereas the N-terminal and the C-terminal regions are suggested to play a role in oligomerization [7,14,15]. The missense mutation found in family A occurred at an evolutionarily conserved amino acid in the N-terminal region, suggesting that the mutation may impair oligomerization. *CRYGC*, encoding γC-crystallin, plays a crucial role in lens development and the maintenance of lens transparency [16]. The γC-crystallin proteins are tightly folded into two domains, with each domain composed of two exceptionally stable protein structures called Greek-key motifs [17-19]. The relatively loose or partially unfolded structure of mutant γC-crystallin may be susceptible to aggregation and insolubilization, which leads to cataract formation [20]. Ren et al. reported a 5-bp duplication (c.119_123dupGCGGC) within exon 2 of the *CRYGC* gene in patients with autosomal dominant congenital cataract [16]. The c.124delT mutation in family B and the c.119_123dupGCGGC mutation cause truncation within the first domain, and are likely to lead to similar effects.

We pooled DNA from one unaffected case (MC13b) and one affected case (MC13) in family B because of the error in information transfer (the affected person was switched from MC13a to MC13b), theoretically resulting in one mutant allele among four existing alleles. However, we still detected a pathological variant (c.124delT), which was present at an allele frequency of 36.47% in our sequence reads. This is consistent with recent reports that WES can detect mosaic pathogenic mutations present at allele frequencies as low as 3.6% to 8% [21-24]. WES has been proven to be useful in clinical diagnosis and personalized disease-risk profiling [10]. Several groups applied WES to successfully identify de novo pathogenic mutations in sporadic patients, supporting its utility [25-27]. WES is particularly useful for small pedigrees, in which linkage mapping is difficult, for cases with previously unrecognized or atypical phenotypes, and for disorders with high genetic heterogeneity [28,29]. Because congenital cataract shows wide phenotypic variability and genetic heterogeneity, WES is appropriate to reach a correct genetic diagnosis. In fact, we performed WES in three families showing congenital cataract and identified pathogenic mutations in two as described here, supporting that WES is quite powerful for dissecting the genetic basis of congenital cataract. Because the cost of WES is now falling, it is likely to be provided as a clinical service in the very near future and will provide useful information for genetic counseling and family planning in congenital cataract. In conclusion, WES successfully identified pathogenic mutations in two Korean families with congenital cataract, clearly demonstrating the efficiency and diagnostic utility of this technique in congenital cataract.

APPENDIX 1.

Whole-exome sequencing performance. To access the data, click or select the words "Appendix 1."

APPENDIX 2.

Candidate genes for congenital cataract. To access the data, click or select the words "Appendix 2."

ACKNOWLEDGMENTS

We would like to thank the patients and their families for their participation in this study. This work was supported by research grants from the Ministry of Health, Labour and Welfare (H Saitsu, N Miyake, N Matsumoto) (12944231) and the Japan Science and Technology Agency (N Matsumoto) (11800122); a Grant-in-Aid for Scientific Research on Innovative Areas-(Transcription cycle)-from the Ministry of Education, Culture, Sports, Science and Technology of Japan (N Matsumoto) (12906972); a Grant-in-Aid for Scientific Research from the Japan Society for the Promotion of Science (N Matsumoto) (12940356); a Grant-in-Aid for Young Scientists from the Japan Society for the Promotion of Science (H Saitsu, N Miyake); and a grant from the Takeda Science Foundation (N Miyake and N Matsumoto).

REFERENCES

1. Rahi JS, Dezateux C. Measuring and interpreting the incidence of congenital ocular anomalies: lessons from a national study of congenital cataract in the UK. Invest Ophthalmol Vis Sci 2001; 42:1444-8. [PMID: 11381045].
2. Chan WH, Biswas S, Ashworth JL, Lloyd IC. Congenital and infantile cataract: aetiology and management. Eur J Pediatr 2012; 171:625-30. [PMID: 22383071].
3. Churchill A, Graw J. Clinical and experimental advances in congenital and paediatric cataracts. Philos Trans R Soc Lond B Biol Sci 2011; 366:1234-49. [PMID: 21402583].
4. Bermejo E, Martinez-Frias ML. Congenital eye malformations: clinical-epidemiological analysis of 1,124,654 consecutive births in Spain. Am J Med Genet 1998; 75:497-504. [PMID: 9489793].
5. Hejtmancik JF. Congenital cataracts and their molecular genetics. Semin Cell Dev Biol 2008; 19:134-49. [PMID: 18035564].
6. Santhiya ST, Soker T, Klopp N, Illig T, Prakash MV, Selvaraj B, Gopinath PM, Graw J. Identification of a novel, putative cataract-causing allele in *CRYAA* (G98R) in an Indian family. Mol Vis 2006; 12:768-73. [PMID: 16862070].
7. Hansen L, Yao W, Eiberg H, Kjaer KW, Baggesen K, Hejtmancik JF, Rosenberg T. Genetic heterogeneity in microcornea-cataract: five novel mutations in *CRYAA, CRYGD*, and *GJA8*. Invest Ophthalmol Vis Sci 2007; 48:3937-44. [PMID: 17724170].
8. Huang B, He W. Molecular characteristics of inherited congenital cataracts. Eur J Med Genet 2010; 53:347-57. [PMID: 20624502].
9. Weisschuh N, Aisenbrey S, Wissinger B, Riess A. Identification of a novel *CRYBB2* missense mutation causing congenital autosomal dominant cataract. Mol Vis 2012; 18:174-80. [PMID: 22312185].
10. Bamshad MJ, Ng SB, Bigham AW, Tabor HK, Emond MJ, Nickerson DA, Shendure J. Exome sequencing as a tool for Mendelian disease gene discovery. Nat Rev Genet 2011; 12:745-55. [PMID: 21946919].
11. Miyamoto T, Yu YS, Sato H, Hayashi H, Sakugawa N, Ishikawa M, Sengoku K. Mutational analysis of the human *MBX* gene in four Korean families demonstrating microphthalmia with congenital cataract. Turk J Pediatr 2007; 49:334-6. [PMID: 17990594].
12. Li H, Ruan J, Durbin R. Mapping short DNA sequencing reads and calling variants using mapping quality scores. Genome Res 2008; 18:1851-8. [PMID: 18714091].
13. Litt M, Kramer P, LaMorticella DM, Murphey W, Lovrien EW, Weleber RG. Autosomal dominant congenital cataract associated with a missense mutation in the human alpha crystallin gene *CRYAA*. Hum Mol Genet 1998; 7:471-4. [PMID: 9467006].
14. Fu L, Liang JJ. Detection of protein-protein interactions among lens crystallins in a mammalian two-hybrid system assay. J Biol Chem 2002; 277:4255-60. [PMID: 11700327].
15. Ghosh JG, Clark JI. Insights into the domains required for dimerization and assembly of human alphaB crystallin. Protein Sci 2005; 14:684-95. [PMID: 15722445].
16. Ren Z, Li A, Shastry BS, Padma T, Ayyagari R, Scott MH, Parks MM, Kaiser-Kupfer MI, Hejtmancik JF. A 5-base insertion in the gammaC-crystallin gene is associated with autosomal dominant variable zonular pulverulent cataract. Hum Genet 2000; 106:531-7. [PMID: 10914683].
17. Héon E, Priston M, Schorderet DF, Billingsley GD, Girard PO, Lubsen N, Munier FL. The gamma-crystallins and human cataracts: a puzzle made clearer. Am J Hum Genet 1999; 65:1261-7. [PMID: 10521291].
18. Yao K, Jin C, Zhu N, Wang W, Wu R, Jiang J, Shentu X. A nonsense mutation in *CRYGC* associated with autosomal dominant congenital nuclear cataract in a Chinese family. Mol Vis 2008; 14:1272-6. [PMID: 18618005].
19. Zhang L, Fu S, Ou Y, Zhao T, Su Y, Liu P. A novel nonsense mutation in *CRYGC* is associated with autosomal dominant congenital nuclear cataracts and microcornea. Mol Vis 2009; 15:276-82. [PMID: 19204787].
20. Talla V, Narayanan C, Srinivasan N, Balasubramanian D. Mutation causing self-aggregation in human gammaC-crystallin leading to congenital cataract. Invest Ophthalmol Vis Sci 2006; 47:5212-7. [PMID: 17122105].
21. Lindhurst MJ, Sapp JC, Teer JK, Johnston JJ, Finn EM, Peters K, Turner J, Cannons JL, Bick D, Blakemore L, Blumhorst C, Brockmann K, Calder P, Cherman N, Deardorff MA, Everman DB, Golas G, Greenstein RM, Kato BM, Keppler-Noreuil KM, Kuznetsov SA, Miyamoto RT, Newman K, Ng D, O'Brien K, Rothenberg S, Schwartzentruber DJ, Singhal V, Tirabosco R, Upton J, Wientroub S, Zackai EH, Hoag K, Whitewood-Neal T, Robey PG, Schwartzberg PL, Darling TN, Tosi LL, Mullikin JC, Biesecker LG. A mosaic activating mutation in *AKT1* associated with the Proteus syndrome. N Engl J Med 2011; 365:611-9. [PMID: 21793738].

22. Lee JH, Huynh M, Silhavy JL, Kim S, Dixon-Salazar T, Heiberg A, Scott E, Bafna V, Hill KJ, Collazo A, Funari V, Russ C, Gabriel SB, Mathern GW, Gleeson JG. De novo somatic mutations in components of the PI3K–AKT3-mTOR pathway cause hemimegalencephaly. Nat Genet 2012; 44:941-5. [PMID: 22729223].

23. Lindhurst MJ, Parker VE, Payne F, Sapp JC, Rudge S, Harris J, Witkowski AM, Zhang Q, Groeneveld MP, Scott CE, Daly A, Huson SM, Tosi LL, Cunningham ML, Darling TN, Geer J, Gucev Z, Sutton VR, Tziotzios C, Dixon AK, Helliwell T, O'Rahilly S, Savage DB, Wakelam MJ, Barroso I, Biesecker LG, Semple RK. Mosaic overgrowth with fibroadipose hyperplasia is caused by somatic activating mutations in *PIK3CA*. Nat Genet 2012; 44:928-33. [PMID: 22729222].

24. Pagnamenta AT, Lise S, Harrison V, Stewart H, Jayawant S, Quaghebeur G, Deng AT, Murphy VE, Sadighi Akha E, Rimmer A, Mathieson I, Knight SJ, Kini U, Taylor JC, Keays DA. Exome sequencing can detect pathogenic mosaic mutations present at low allele frequencies. J Hum Genet 2012; 57:70-2. [PMID: 22129557].

25. Vissers LE, de Ligt J, Gilissen C, Janssen I, Steehouwer M, de Vries P, van Lier B, Arts P, Wieskamp N, del Rosario M, van Bon BW, Hoischen A, de Vries BB, Brunner HG, Veltman JA. A de novo paradigm for mental retardation. Nat Genet 2010; 42:1109-12. [PMID: 21076407].

26. Awadalla P, Gauthier J, Myers RA, Casals F, Hamdan FF, Griffing AR, Cote M, Henrion E, Spiegelman D, Tarabeux J, Piton A, Yang Y, Boyko A, Bustamante C, Xiong L, Rapoport JL, Addington AM, DeLisi JL, Krebs MO, Joober R, Millet B, Fombonne E, Mottron L, Zilversmit M, Keebler J, Daoud H, Marineau C, Roy-Gagnon MH, Dube MP, Eyre-Walker A, Drapeau P, Stone EA, Lafreniere RG, Rouleau GA. Direct measure of the de novo mutation rate in autism and schizophrenia cohorts. Am J Hum Genet 2010; 87:316-24. [PMID: 20797689].

27. O'Roak BJ, Deriziotis P, Lee C, Vives L, Schwartz JJ, Girirajan S, Karakoc E, Mackenzie AP, Ng SB, Baker C, Rieder MJ, Nickerson DA, Bernier R, Fisher SE, Shendure J, Eichler EE. Exome sequencing in sporadic autism spectrum disorders identifies severe de novo mutations. Nat Genet 2011; 43:585-9. [PMID: 21572417].

28. Majewski J, Wang Z, Lopez I, Al Humaid S, Ren H, Racine J, Bazinet A, Mitchel G, Braverman N, Koenekoop RK. A new ocular phenotype associated with an unexpected but known systemic disorder and mutation: novel use of genomic diagnostics and exome sequencing. J Med Genet 2011; 48:593-6. [PMID: 21862673].

29. Tsurusaki Y, Okamoto N, Suzuki Y, Doi H, Saitsu H, Miyake N, Matsumoto N. Exome sequencing of two patients in a family with atypical X-linked leukodystrophy. Clin Genet 2011; [PMID: 21644943].

Articles are provided courtesy of Emory University and the Zhongshan Ophthalmic Center, Sun Yat-sen University, P.R. China. The print version of this article was created on 18 February 2013. This reflects all typographical corrections and errata to the article through that date. Details of any changes may be found in the online version of the article.

nature genetics

De novo mutations in the autophagy gene *WDR45* cause static encephalopathy of childhood with neurodegeneration in adulthood

Hirotomo Saitsu[1,10], Taki Nishimura[2,3,10], Kazuhiro Muramatsu[4,10], Hirofumi Kodera[1], Satoko Kumada[5], Kenji Sugai[6], Emi Kasai-Yoshida[5], Noriko Sawaura[4], Hiroya Nishida[7], Ai Hoshino[7], Fukiko Ryujin[8], Seiichiro Yoshioka[8], Kiyomi Nishiyama[1], Yukiko Kondo[1], Yoshinori Tsurusaki[1], Mitsuko Nakashima[1], Noriko Miyake[1], Hirokazu Arakawa[4], Mitsuhiro Kato[9], Noboru Mizushima[2,3] & Naomichi Matsumoto[1]

Static encephalopathy of childhood with neurodegeneration in adulthood (SENDA) is a recently established subtype of neurodegeneration with brain iron accumulation (NBIA)[1–3]. By exome sequencing, we found *de novo* heterozygous mutations in *WDR45* at Xp11.23 in two individuals with SENDA, and three additional *WDR45* mutations were identified in three other subjects by Sanger sequencing. Using lymphoblastoid cell lines (LCLs) derived from the subjects, aberrant splicing was confirmed in two, and protein expression was observed to be severely impaired in all five. *WDR45* encodes WD-repeat domain 45 (WDR45). WDR45 (also known as WIPI4) is one of the four mammalian homologs of yeast Atg18, which has an important role in autophagy[4,5]. Lower autophagic activity and accumulation of aberrant early autophagic structures were demonstrated in the LCLs of the affected subjects. These findings provide direct evidence that an autophagy defect is indeed associated with a neurodegenerative disorder in humans.

NBIA is a heterogeneous group of neurodegenerative diseases that are characterized by a prominent extrapyramidal movement disorder, intellectual deterioration and deposition of iron in the basal ganglia[1–3]. Mutations in several genes involved in diverse cellular processes cause NBIA[6]. SENDA is a recently established subtype of NBIA. SENDA begins with early childhood psychomotor retardation, which remains static until adulthood. Then, during their twenties to early thirties, affected individuals develop sudden-onset progressive dystonia-parkinsonism and dementia. In addition to iron deposition in the globus pallidus and substantia nigra, individuals with SENDA have a distinct pattern on brain magnetic resonance images (MRI) of T1-weighted signal hyperintensity of the substantia nigra, with a central band of hypointensity[1–3,6,7]. SENDA is always sporadic[6,7], suggesting the involvement of *de novo* mutations or autosomal recessive traits. To identify *de novo* or recessive mutations, family-based exome sequencing was performed including the affected individual, an unaffected sibling and the unaffected parents.

A total of 180 and 187 rare protein-altering and splice-site variants were identified per affected subject, which were absent in dbSNP135 data and in 88 in-house control exomes (**Supplementary Table 1**). All genes in each subject were surveyed for *de novo* mutations and compound heterozygous or homozygous mutations that were consistent with an autosomal recessive trait in each family (**Supplementary Table 2**). Two *de novo* and one autosomal recessive candidate mutations were found in subject 1, and a *de novo* candidate mutation was found in subject 2. Only mutations in *WDR45* at Xp11.23, encoding WDR45 (referred to here as WIPI4), were common in the two subjects. A canonical splice-site mutation (c.439+1G>T) was found in subject 1, and a synonymous mutation located at the last base of exon 8 (c.516G>C) was found in subject 2, both of which occurred *de novo* (**Fig. 1a**). Sanger sequencing of *WDR45* in three other affected subjects identified one nonsense and two frameshift mutations (**Fig. 1a**). The c.1033_1034dupAA mutation in subject 5 occurred *de novo*. Parental samples for the other two subjects were unavailable. None of the five mutations were found in 6,500 National Heart, Lung, and Blood Institute (NHLBI) exomes or among our 212 in-house control exomes. All subjects with a *WDR45* mutation are female.

To examine the effects of the mutations on *WDR45* transcription, RT-PCR and sequencing were performed on total RNA extracted from the LCLs of subjects. The c.439+1G>T mutation in subject 1 and the c.516G>C mutation in subject 2 caused 24-bp in-frame and 22-bp

[1]Department of Human Genetics, Graduate School of Medicine, Yokohama City University, Yokohama, Japan. [2]Department of Physiology and Cell Biology, Graduate School and Faculty of Medicine, Tokyo Medical and Dental University, Tokyo, Japan. [3]Department of Biochemistry and Molecular Biology, Graduate School and Faculty of Medicine, The University of Tokyo, Tokyo, Japan. [4]Department of Pediatrics, Gunma University Graduate School of Medicine, Gunma, Japan. [5]Department of Neuropediatrics, Tokyo Metropolitan Neurological Hospital, Tokyo, Japan. [6]Department of Child Neurology, National Center of Neurology and Psychiatry, Tokyo, Japan. [7]Department of Pediatrics, National Rehabilitation Center for Children with Disabilities, Tokyo, Japan. [8]Department of Pediatrics, Shiga University of Medical Science, Shiga, Japan. [9]Department of Pediatrics, Yamagata University Faculty of Medicine, Yamagata, Japan. [10]These authors contributed equally to this work. Correspondence should be addressed to H.S. (hsaitsu@yokohama-cu.ac.jp), N. Mizushima (nmizu@m.u-tokyo.ac.jp) or N. Matsumoto (naomat@yokohama-cu.ac.jp).

Received 24 October 2012; accepted 29 January 2013; published online 24 February 2013; doi:10.1038/ng.2562

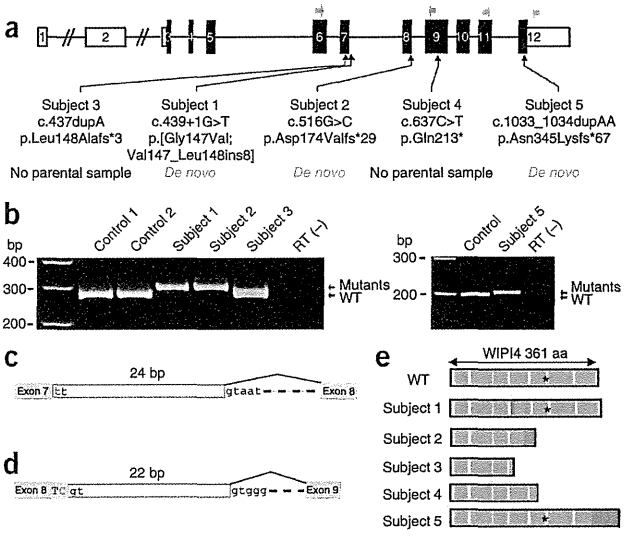

Figure 1 Heterozygous *WDR45* mutations in individuals with SENDA. (**a**) Schematic of *WDR45*, which comprises 12 exons (rectangles). The UTRs and coding region are shown in white and black, respectively. Three mutations were confirmed as *de novo*; the others were unable to be confirmed because parental samples were unavailable. Blue and green arrows indicate the locations of the two sets of primers used in mRNA analysis. (**b**) RT-PCR analysis using the blue primer set (left) and green primer set (right) from **a**. Whereas control cDNA samples showed a single product corresponding to the wild-type allele (WT), an apparently longer product was observed in subjects 1, 2 and 5, indicating that only the transcripts from the mutant allele were expressed. In subject 3, both wild-type and mutant alleles were expressed. Template without reverse transcriptase was used as a negative control, RT(–). (**c**) Schematic of the mutant transcript resulting from the c.439+1G>T mutation (red) in subject 1. A 24-bp insertion caused by the use of a cryptic splice donor site within intron 7 was observed, resulting in a p.Gly147Val substitution followed by an in-frame eight-amino-acid insertion (p.[Gly147Val; Val147_Leu148ins8]). (**d**) Schematic of the mutant transcript resulting from the c.516G>C mutation (red) in subject 2. A 22-bp insertion from the use of a cryptic splice donor site within intron 8 was observed, leading to a frameshift (p.Asp174Valfs*29). (**e**) Schematic of mutant WIPI4 proteins. β-propeller structures and additional residues caused by mutations are colored in blue and red, respectively. The amino-acid residues of the mutant protein predicted from cDNA sequences are shown in relation to seven–β propeller structures[13–15]. An asterisk indicates the position of the FRRG motifs.

frameshift insertions, respectively (**Fig. 1b–d** and **Supplementary Fig. 1**). The c.437dupA, c.637C>T and c.1033_1034dupAA mutations were confirmed in the transcripts (**Fig. 1b** and **Supplementary Fig. 1**). Theoretically, mutant WIPI4 would be severely truncated in subjects 2, 3 and 4 and relatively conserved in subjects 1 and 5 (**Fig. 1e**). As human female cells are subject to X-chromosome inactivation, subjects with a *WDR45* mutation may have two cell populations: one expressing a wild-type allele and the other expressing a mutant allele. Notably, whereas both wild-type and mutant alleles were expressed in the LCLs of subject 3, the LCLs of the other four affected subjects exclusively expressed mutant transcripts, suggesting that the wild-type alleles underwent X inactivation in most cells (**Fig. 1b** and **Supplementary Fig. 1**). In fact, X-inactivation analysis with genomic DNA from peripheral leukocytes showed a skewed pattern in subjects 2, 4 and 5 (analysis was non-informative in subject 1) (**Supplementary Table 3**). However, it is unknown whether the wild-type allele underwent X inactivation in brain tissues as in LCLs and leukocytes from the subjects.

The clinical features of the individuals with SENDA possessing *WDR45* mutations are summarized in **Table 1** (see also the **Supplementary Note**). Subjects 1 and 3 have been described recently[7,8]. These individuals showed psychomotor developmental delay from infancy and severe intellectual disability, while their motor function gradually developed. In adulthood, severe progressive dystonia-parkinsonism and dementia developed. Four of the subjects became bedridden within a few years of onset of cognitive decline. In all subjects, blood concentrations of ceruloplasmin, copper, iron, ferritin and lactate acid were normal. Brain MRI showed T1-weighted signal hyperintensity in the substantia nigra with a central T1-weighted hypointensity band (**Fig. 2a–e**) and T2-weighted signal hypointensity, suggesting iron deposition in the globus pallidus and substantia nigra (**Fig. 2f–h**), which are characteristic of SENDA. In addition, significant cerebral atrophy was found (**Fig. 2i,j**). Substantial differences in the severity of clinical findings were not observed among the five subjects.

WIPI1, WIPI2, WIPI3 and WIPI4, mammalian Atg18 homologs, have an important role in the autophagy pathway[4,5]. Autophagy is the major intracellular degradation system by which cytoplasmic materials are enclosed by double-membrane structures called autophagosomes and subsequently delivered to lysosomes for degradation[9]. More than 30 autophagy-related (ATG) genes have been identified in yeast[10,11], many of which are conserved in higher eukaryotes and are essential for the formation of the autophagosome[10,12]. These factors include subunits of the class III phosphatidylinositol 3-kinase complex, and generation of the lipid phosphatidylinositol 3-phosphate is essential for autophagosome formation. Atg18 in yeast and WIPI subunits in mammals associate with membranes through a phosphoinositide-binding motif (FRRG) within a seven–β propeller structure[13–15]. Atg18 and WIPI proteins also interact with Atg2 and its homologs in yeast and mammalian cells, respectively[16,17]. Autophagic activity in relation to WIPI4 expression was examined using LCLs from the subjects. Immunoblot analysis of WIPI4 showed lower expression in all five subjects compared to unaffected individuals (**Fig. 3a**). Although mutant WIPI4 protein sequence was relatively conserved in subjects 1 and 5, the expression of mutant WIPI4 in both subjects was severely decreased, similar to that of subjects 2, 3 and 4, in whom mutant WIPI4 was truncated. This suggests that all the mutant proteins are structurally unstable and undergo degradation. To examine the effect of the *WDR45* mutations on autophagy, an autophagic flux assay was performed using LCLs. When lysosomal degradation was blocked by the lysosomal inhibitor chloroquine, the amount of LC3-II (the membrane-bound form) was higher than in cells without the inhibitor, as for control LCLs (**Fig. 3b** and **Supplementary Fig. 2**)[18]. The differences in LC3-II amounts between samples with and without chloroquine represent the amount of LC3 on autophagic structures delivered to lysosomes for degradation[18]. In the LCLs from affected subjects, accumulation of LC3-II was observed, even under normal conditions, which was more apparent when autophagy was induced by the mTORC1 inhibitor Torin1 (**Supplementary Fig. 2a–d**). The increase in the LC3-II amount by concomitant chloroquine treatment was significant or tended to be suppressed in the LCLs from affected subjects, suggesting that the autophagic flux was blocked, probably incompletely, at an intermediate step of autophagosome formation (**Fig. 3b** and **Supplementary Fig. 2e**).

Consistent with the immunoblot analysis, immunofluorescence microscopy showed the accumulation of LC3-containing autophagic

Table 1 Clinical features of subjects with SENDA with a *WDR45* mutation

	Subject 1	Subject 2	Subject 3	Subject 4	Subject 5
Age	33 years	28 years	40 years	51 years	33 years
Sex	Female	Female	Female	Female	Female
Mutation	c.439+1G>T	c.516G>C	c.437dupA	c.637C>T	c.1033_1034dupAA
Protein alteration	p.[Gly147Val; Val147_Leu148ins8]	p.Asp174Valfs*29	p.Leu148Alafs*3	p.Gln213*	p.Asn345Lysfs*67
Neurological symptoms					
Current status	Bedridden	Wheelchair	Bedridden	Bedridden	Bedridden
Initial symptom	Psychomotor retardation	Psychomotor retardation	Psychomotor retardation	Psychomotor retardation	Psychomotor retardation
Initial walking	3 years	2 years 7 months	2 years 2 months	1 year 6 months	1 year 6 months
Speech ability	No word	One word	No word	Two-word sentences	Few words
Cognitive dysfunction during childhood	Nonprogressive	Nonprogressive	Nonprogressive	Nonprogressive	Nonprogressive
Start of cognitive decline	26 years	25 years	30 years	24 years	23 years
Period until bedridden after decline	4 years	–	3 years	1 year	6 years
Dystonia	+	+	+	+	+
Parkinsonism	Rigidity, akinesia	Rigidity, akinesia	Rigidity	Rigidity	Rigidity, tremor, impairment of postural reflex
Progressive dementia during adulthood	+	+	+	+	+
Psychiatric symptoms	Aggressive behaviors	Aggressive behaviors	None	None	Anxiety
Epileptic seizure	+	+	FS	None	+
Radiological features					
MRI					
Iron deposition	Globus pallidus, substantia nigra	Globus pallidus, substantia nigra	Globus pallidus, substantia nigra	Globus pallidus, substantia nigra	Globus pallidus, substantia nigra
Central band of T1 hypointensity	+	+	+	+	+
Cerebral atrophy	Moderate at 25 years, remarkable at 32 and 33 years	Moderate at 25 and 27 years	Mild at 33 years, remarkable at 39 years	Mild at 27 years, remarkable at 46 years	Remarkable at 33 years
Eye of the tiger sign	–	–	–	–	–
White matter involvement	–	–	–	–	–
Cerebellar atrophy	Mild at 25, 32 and 33 years	Mild at 25 and 27 years	Mild at 33 and 39 years	Mild at 27 and 46 years	Mild at 33 years
CT findings	High density in globus pallidus	Mild high density in substantia nigra	High density in substantia nigra	High density in ventral midbrain	High density in globus pallidus
Neurophysiological examination					
EEG	Bilateral frontal spike	Bilateral frontal spike, low voltage, slow wave	Low voltage	Abnormal	Abnormal
EMG	NE	NE	Dystonic pattern	Normal	NE
VEP	Normal	NE	Prolonged P100 latency	NE	Normal
ABR	Low amplitude, normal latency	NE	No response at 100 dB	NE	NE

FS, febrile seizure; EEG, electroencephalogram; EMG, electromyogram; VEP, visual evoked potential; ABR, auditory brainstem response; NE, not examined.

structures in the LCLs from affected subjects, some of which were abnormally enlarged compared with those observed in control LCLs (**Fig. 3c,d**). Therefore, we examined whether these LC3-positive structures in fact included premature or abnormal autophagic structures. A recent study showed that knockdown of *Wdr45* in rat kidney cells and mutation in *epg-6* (encoding a WIPI4 homolog)

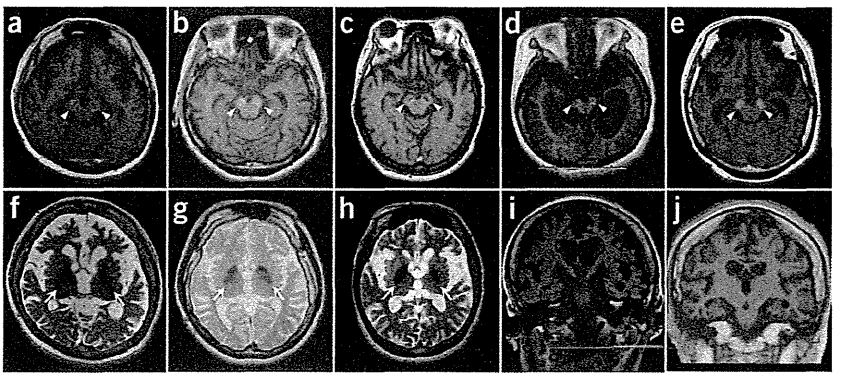

Figure 2 Brain MRIs at 3.0 T and 1.5 T. (**a–e**) T1-weighted imaging shows hyperintensity of the substantia nigra with a central band of T1-weighted hypointensity (arrowheads). Images are shown for subject 1 at 33 years (**a**), subject 2 at 25 years (**b**), subject 3 at 39 years (**c**), subject 4 at 46 years (**d**) and subject 5 at 33 years (**e**). (**f–h**) T2-weighted imaging shows marked hypointensity of the globus pallidus (arrows), suggesting iron deposition. Cerebral atrophy and mild cerebellar atrophy are also seen. Images are shown for subject 1 (**f**), subject 2 (**g**) and subject 3 (**h**). (**i,j**) The fluid attenuated inversion recovery (FLAIR) image of subject 1 (**i**) and the T1-weighted FLAIR coronal image of subject 2 (**j**) also show cerebral atrophy.

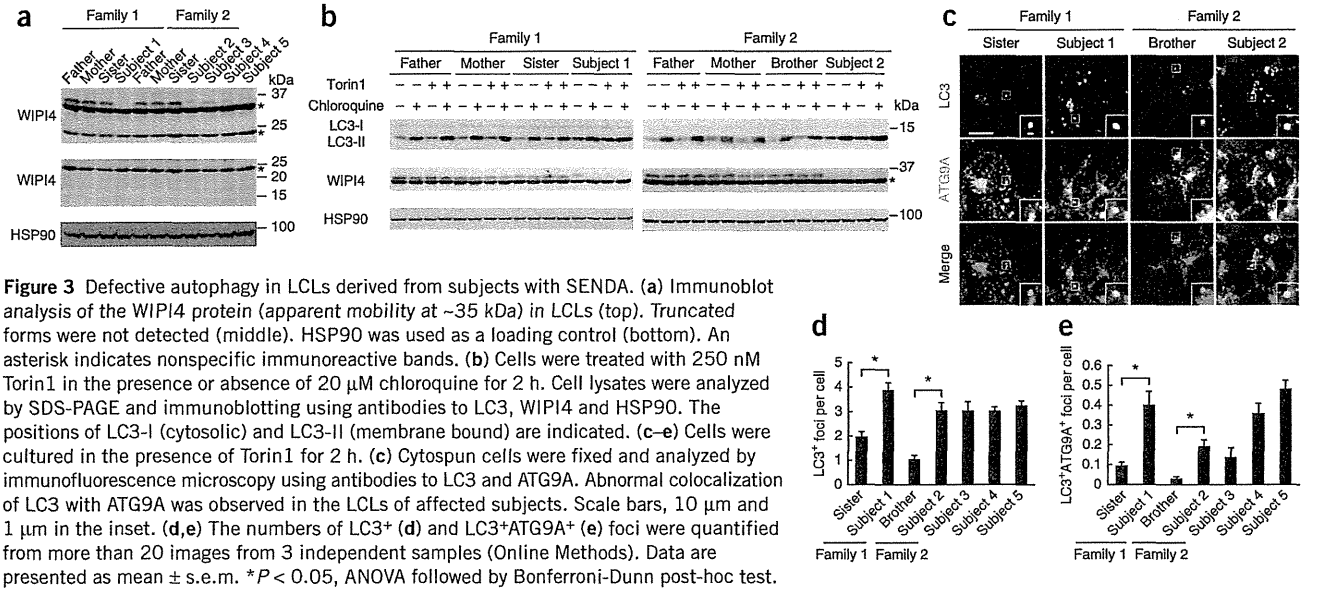

Figure 3 Defective autophagy in LCLs derived from subjects with SENDA. (**a**) Immunoblot analysis of the WIPI4 protein (apparent mobility at ~35 kDa) in LCLs (top). Truncated forms were not detected (middle). HSP90 was used as a loading control (bottom). An asterisk indicates nonspecific immunoreactive bands. (**b**) Cells were treated with 250 nM Torin1 in the presence or absence of 20 μM chloroquine for 2 h. Cell lysates were analyzed by SDS-PAGE and immunoblotting using antibodies to LC3, WIPI4 and HSP90. The positions of LC3-I (cytosolic) and LC3-II (membrane bound) are indicated. (**c–e**) Cells were cultured in the presence of Torin1 for 2 h. (**c**) Cytospun cells were fixed and analyzed by immunofluorescence microscopy using antibodies to LC3 and ATG9A. Abnormal colocalization of LC3 with ATG9A was observed in the LCLs of affected subjects. Scale bars, 10 μm and 1 μm in the inset. (**d,e**) The numbers of $LC3^+$ (**d**) and $LC3^+ATG9A^+$ (**e**) foci were quantified from more than 20 images from 3 independent samples (Online Methods). Data are presented as mean ± s.e.m. $^*P < 0.05$, ANOVA followed by Bonferroni-Dunn post-hoc test.

in *Caenorhabditis elegans* cause accumulation of early autophagic structures[5]. One supposed function of WIPI4 (Epg-6) is to regulate the distribution of ATG9A-marked vesicles[5], which transiently localize to the autophagosome formation site and induce autophagosome formation[19,20]. ATG9A is absent from completed autophagosomes in mammalian cells; therefore, colocalization of ATG9A and LC3 is rare. However, enlarged structures positive for both ATG9A and LC3 accumulated in LCLs from all five subjects (**Fig. 3c,e**), indicating improper autophagosome formation.

The importance of the housekeeping activity of autophagy in neurons, as well as the ubiquitin-proteasome system, has been demonstrated in mice. Mice lacking autophagy in the central nervous system developed progressive motor and behavioral deficits[21,22]. Histologically, inclusion bodies containing polyubiquitinated proteins were observed in neurons, and their size and number increased with age[21,22]. Neuronal cell death was observed in subsets of neurons[21,22], implying that the impairment of autophagy contributes to the pathogenesis of neurodegenerative disorders. Indeed, dysregulation of autophagy has been suggested in various neurodegenerative disorders in humans[23]. In addition, mutations in *PARK2* and *PINK1*, both of which cause familial Parkinson's disease[24,25], impair the selective autophagic degradation of damaged mitochondria, called mitophagy (PARK2, also called Parkin, is recruited to damaged mitochondria in a PINK1-dependent manner)[26,27]. However, a direct link between the core autophagy machinery and human neurodegenerative disorders has not been reported. Here, we showed that mutations in *WDR45*, a core autophagy gene, result in a neurodegenerative disorder. Notably, the autophagy defects were partial, implying that some autophagic activity could be maintained in the neurons of affected subjects. We hypothesize that this might be a possible explanation of why childhood intellectual disability in individuals with SENDA remains static until adulthood, unlike in other forms of NBIA[1–3]. In contrast to heterozygous *WDR45* mutations in females, hemizygous germline mutations in males, leading to the expression of mutant *WDR45* in all cells, possibly cause lethal phenotypes from complete loss of *WDR45* function, as mice defective in autophagy die shortly after birth[28–32]. While this paper was under review, Haack *et al.* reported *WDR45* mutations in 20 subjects, including 3 males, 1 of whom possessed a mutation that was somatic mosaic, supporting the idea that male germline mutations could be lethal[33].

WDR45 is widely expressed in human tissues, with the highest expression found in skeletal muscle[34]. Nevertheless, SENDA phenotypes seem to be limited to the brain. These facts may reflect cell type–dependent differences: autophagy could be more important in neurons (non-dividing, terminally differentiated cells) than in LCLs (rapidly dividing cells). In addition, it is possible that the other WIPI homologs (WIPI1, WIPI2 and WIPI3) could compensate for the deficiency in WIPI4 in a cell type–dependent manner, and the relative contribution of WIPI4 among WIPI factors may be high in neurons.

In conclusion, heterozygous mutations of X-linked *WDR45*, a core autophagy gene, were identified in SENDA, providing direct evidence that an autophagy defect is indeed associated with a neurodegenerative disorder in humans.

URLs. NHLBI Exome Sequencing Project, http://evs.gs.washington.edu/EVS/; Picard, http://picard.sourceforge.net/; SAMtools, http://samtools.sourceforge.net/; dbSNP, http://www.ncbi.nlm.nih.gov/projects/SNP/.

METHODS

Methods and any associated references are available in the online version of the paper.

Accession codes. Reference sequences are available from GenBank for *Homo sapiens WDR45* transcript variant 1 mRNA (NM_007075.3) and WIPI4 isoform 1 (NP_009006.2).

Note: Supplementary information is available in the online version of the paper.

ACKNOWLEDGMENTS

We would like to thank the individuals with SENDA and their families for their participation in this study. We thank M. Shiina and K. Ogata for their helpful comments on the protein structure. This work was supported by research grants from the Ministry of Health, Labour and Welfare (H.S., N. Miyake and N. Matsumoto), the Japan Science and Technology Agency (N. Matsumoto) and the Strategic Research Program for Brain Sciences (N. Matsumoto) and by a Grant-in-Aid for Scientific Research on Innovative Areas (Transcription Cycle) from the Ministry of Education, Culture, Sports, Science and Technology of Japan

(N. Matsumoto), a Grant-in-Aid for Scientific Research from the Japan Society for the Promotion of Science (N. Matsumoto), a Grant-in-Aid for Young Scientists from the Japan Society for the Promotion of Science (H.S. and N. Miyake), the Funding Program for Next-Generation World-Leading Researchers (N. Mizushima) and a grant from the Takeda Science Foundation (N. Miyake, N. Mizushima and N. Matsumoto).

AUTHOR CONTRIBUTIONS

H.S., N. Mizushima and N. Matsumoto designed and directed the study. H.S., T.N., K.M., N. Mizushima and N. Matsumoto wrote the manuscript. K.M., S.K., K.S., E.K.-Y., N.S., H.N., A.H., F.R., S.Y., H.A. and M.K. collected samples and provided the subjects' clinical information. H.S., H.K., K.N., Y.T., M.N. and N. Miyake performed exome sequencing and Sanger sequencing. H.S. and K.N. performed the RNA analysis. Y.K. performed the X-inactivation analysis. T.N. and N. Mizushima analyzed protein expression and autophagic activity.

COMPETING FINANCIAL INTERESTS

The authors declare no competing financial interests.

1. Gregory, A., Polster, B.J. & Hayflick, S.J. Clinical and genetic delineation of neurodegeneration with brain iron accumulation. *J. Med. Genet.* **46**, 73–80 (2009).
2. Kruer, M.C. *et al.* Neuroimaging features of neurodegeneration with brain iron accumulation. *AJNR Am. J. Neuroradiol.* **33**, 407–414 (2012).
3. Schneider, S.A. & Bhatia, K.P. Syndromes of neurodegeneration with brain iron accumulation. *Semin. Pediatr. Neurol.* **19**, 57–66 (2012).
4. Polson, H.E. *et al.* Mammalian Atg18 (WIPI2) localizes to omegasome-anchored phagophores and positively regulates LC3 lipidation. *Autophagy* **6**, 506–522 (2010).
5. Lu, Q. *et al.* The WD40 repeat PtdIns(3)P-binding protein EPG-6 regulates progression of omegasomes to autophagosomes. *Dev. Cell* **21**, 343–357 (2011).
6. Gregory, A. & Hayflick, S.J. Genetics of neurodegeneration with brain iron accumulation. *Curr. Neurol. Neurosci. Rep.* **11**, 254–261 (2011).
7. Kimura, Y. *et al.* MRI, MR spectroscopy, and diffusion tensor imaging findings in patient with static encephalopathy of childhood with neurodegeneration in adulthood (SENDA). *Brain Dev.* published online; doi:10.1016/j.braindev.2012.07.008 (11 August 2012).
8. Kasai-Yoshida, E. *et al.* First video report of static encephalopathy of childhood with neurodegeneration in adulthood. *Mov. Disord.* published online; doi:10.1002/mds.25158 (6 February 2013).
9. Mizushima, N. & Komatsu, M. Autophagy: renovation of cells and tissues. *Cell* **147**, 728–741 (2011).
10. Nakatogawa, H., Suzuki, K., Kamada, Y. & Ohsumi, Y. Dynamics and diversity in autophagy mechanisms: lessons from yeast. *Nat. Rev. Mol. Cell Biol.* **10**, 458–467 (2009).
11. Xie, Z. & Klionsky, D.J. Autophagosome formation: core machinery and adaptations. *Nat. Cell Biol.* **9**, 1102–1109 (2007).
12. Mizushima, N., Yoshimori, T. & Ohsumi, Y. The role of Atg proteins in autophagosome formation. *Annu. Rev. Cell Dev. Biol.* **27**, 107–132 (2011).
13. Baskaran, S., Ragusa, M.J., Boura, E. & Hurley, J.H. Two-site recognition of phosphatidylinositol 3-phosphate by PROPPINs in autophagy. *Mol. Cell* **47**, 339–348 (2012).
14. Krick, R. *et al.* Structural and functional characterization of the two phosphoinositide binding sites of PROPPINs, a β-propeller protein family. *Proc. Natl. Acad. Sci. USA* **109**, E2042–E2049 (2012).
15. Watanabe, Y. *et al.* Structure-based analyses reveal distinct binding sites for Atg2 and phosphoinositides in Atg18. *J. Biol. Chem.* **287**, 31681–31690 (2012).
16. Suzuki, K., Kubota, Y., Sekito, T. & Ohsumi, Y. Hierarchy of Atg proteins in pre-autophagosomal structure organization. *Genes Cells* **12**, 209–218 (2007).
17. Velikkakath, A.K., Nishimura, T., Oita, E., Ishihara, N. & Mizushima, N. Mammalian Atg2 proteins are essential for autophagosome formation and important for regulation of size and distribution of lipid droplets. *Mol. Biol. Cell* **23**, 896–909 (2012).
18. Mizushima, N., Yoshimori, T. & Levine, B. Methods in mammalian autophagy research. *Cell* **140**, 313–326 (2010).
19. Itakura, E., Kishi-Itakura, C., Koyama-Honda, I. & Mizushima, N. Structures containing Atg9A and the ULK1 complex independently target depolarized mitochondria at initial stages of Parkin-mediated mitophagy. *J. Cell Sci.* **125**, 1488–1499 (2012).
20. Orsi, A. *et al.* Dynamic and transient interactions of Atg9 with autophagosomes, but not membrane integration, are required for autophagy. *Mol. Biol. Cell* **23**, 1860–1873 (2012).
21. Hara, T. *et al.* Suppression of basal autophagy in neural cells causes neurodegenerative disease in mice. *Nature* **441**, 885–889 (2006).
22. Komatsu, M. *et al.* Loss of autophagy in the central nervous system causes neurodegeneration in mice. *Nature* **441**, 880–884 (2006).
23. Menzies, F.M., Moreau, K. & Rubinsztein, D.C. Protein misfolding disorders and macroautophagy. *Curr. Opin. Cell Biol.* **23**, 190–197 (2011).
24. Valente, E.M. *et al.* Hereditary early-onset Parkinson's disease caused by mutations in *PINK1*. *Science* **304**, 1158–1160 (2004).
25. Kitada, T. *et al.* Mutations in the *parkin* gene cause autosomal recessive juvenile parkinsonism. *Nature* **392**, 605–608 (1998).
26. Youle, R.J. & van der Bliek, A.M. Mitochondrial fission, fusion, and stress. *Science* **337**, 1062–1065 (2012).
27. Youle, R.J. & Narendra, D.P. Mechanisms of mitophagy. *Nat. Rev. Mol. Cell Biol.* **12**, 9–14 (2011).
28. Kuma, A. *et al.* The role of autophagy during the early neonatal starvation period. *Nature* **432**, 1032–1036 (2004).
29. Saitoh, T. *et al.* Loss of the autophagy protein Atg16L1 enhances endotoxin-induced IL-1β production. *Nature* **456**, 264–268 (2008).
30. Saitoh, T. *et al.* Atg9a controls dsDNA-driven dynamic translocation of STING and the innate immune response. *Proc. Natl. Acad. Sci. USA* **106**, 20842–20846 (2009).
31. Sou, Y.S. *et al.* The Atg8 conjugation system is indispensable for proper development of autophagic isolation membranes in mice. *Mol. Biol. Cell* **19**, 4762–4775 (2008).
32. Komatsu, M. *et al.* Impairment of starvation-induced and constitutive autophagy in *Atg7*-deficient mice. *J. Cell Biol.* **169**, 425–434 (2005).
33. Haack, T.B. *et al.* Exome sequencing reveals *de novo WDR45* mutations causing a phenotypically distinct, X-linked dominant form of NBIA. *Am. J. Hum. Genet.* **91**, 1144–1149 (2012).
34. Proikas-Cezanne, T. *et al.* WIPI-1α (WIPI49), a member of the novel 7-bladed WIPI protein family, is aberrantly expressed in human cancer and is linked to starvation-induced autophagy. *Oncogene* **23**, 9314–9325 (2004).

ONLINE METHODS

Subjects. We analyzed five Japanese individuals with SENDA. Diagnosis was made on the basis of clinical features, including psychomotor retardation at early childhood that was static for decades and severe progressive dystonia-parkinsonism and dementia after several decades, as well as characteristic findings on brain MRI scans. Genomic DNA was isolated from blood leukocytes according to standard protocols. The Institutional Review Board of Yokohama City University approved the experimental protocols. Informed consent was obtained for all individuals included in this study in agreement with the requirements of Japanese regulations. Clinical information on the subjects with a *WDR45* mutation is presented in **Table 1** and in the **Supplementary Note.**

Mutation screening. Mutation screening of exons 3–12 covering the *WDR45* coding region (of transcript variant 1, GenBank accession NM_007075.3) was performed by direct sequencing. PCR was performed in a 20-μl mixture containing 1 μl of genomic DNA, 1× PCR Buffer for KOD FX NEO, 0.4 mM of each dNTP, 0.3 μM of each primer and 0.4 U of KOD FX NEO polymerase (Toyobo). Details on PCR conditions and primer sequences are given in **Supplementary Table 4.**

Exome sequencing. Genomic DNA was captured using the SureSelect Human All Exon v4 kit (51 Mb; Agilent Technologies) and sequenced with four samples per lane on an Illumina HiSeq2000 with 101-bp paired-end reads. Image analysis and base calling were performed by sequence control software real-time analysis and CASAVA software v1.8 (Illumina). Reads were aligned to GRCh37 with Novoalign (Novocraft Technologies). Duplicate reads were marked using Picard (see URLs) and excluded from downstream analysis. After merging the BAM files of all members in each family using SAMtools, local realignments around indels and base quality score recalibration were performed with the Genome Analysis Toolkit (GATK)[35]. Single-nucleotide variants and small indels were identified using the GATK UnifiedGenotyper and filtered according to the Broad Institute's best-practice guidelines (version 3). Variants registered in dbSNP135, which were not flagged as clinically associated, were excluded. Variants that passed the filters were annotated using ANNOVAR[36].

RNA analysis. LCLs were established from five affected subjects and their family members. RT-PCR using total RNA extracted from LCLs was performed as previously described[37]. Briefly, 4 μg of total RNA extracted with an RNeasy Plus Mini kit (Qiagen) was subjected to reverse transcription, and 2 μl of cDNA was used for PCR. Details on primer sequences and PCR conditions are given in **Supplementary Table 4.** PCR products were electrophoresed in a 10% polyacrylamide gel and sequenced.

X-inactivation analysis. The X-inactivation pattern was studied using the human androgen receptor (HUMARA) assay and a fragile X mental retardation (*FRAXA*) locus methylation assay as previously described[38–40]. Briefly, genomic DNA from the subjects, a control male and a control female was digested with two methylation-sensitive enzymes, HpaII and HhaI. Details on PCR conditions and primer sequences are given in **Supplementary Table 4.** Fluorescently labeled products were analyzed on an ABI PRISM 3500 Genetic Analyzer with GeneMapper Software version 4.0 (Applied Biosystems). X-inactivation ratios of less than or equal to 80:20 were considered to represent a random pattern, ratios greater than 80:20 were considered to represent a skewed pattern, and ratios greater than 90:10 were considered to represent a markedly skewed pattern[38].

Cell culture. LCLs were cultured in RPMI 1640 supplemented with 10% FBS, L-glutamine, tylosin and antibiotic-antimycotic solution in a 5% CO_2 incubator.

Immunoblotting. An affinity-purified rabbit polyclonal antibody against WIPI4 peptide antigen (CFPDNPRKLFEFDTRDNP, amino acids 129–145) was generated by Medical & Biological Laboratories. The specificity of the antibody was tested using lysate from HeLa cells in which *WDR45* was knocked down. For immunoblot analysis, cells were lysed with lysis buffer (50 mM Tris-HCl, pH 7.5, 150 mM NaCl, 1 mM EDTA, 1% Triton X-100, 1 mM phenylmethanesulfonyl fluoride and a protease inhibitor cocktail (Complete EDTA-free protease inhibitor, Roche)). Cell lysates were clarified by centrifugation at 12,000*g* for 20 min and analyzed by SDS-PAGE and immunoblotting using antibodies to WIPI4, LC3 (ref. 41) and HSP90 (BD Transduction Laboratories, 610418). Signal intensities were analyzed using a LAS-3000 mini imaging analyzer and Multi Gauge software version 3.0 (Fujifilm). Contrast and brightness adjustments were applied to the images using Photoshop 7.0.1 (Adobe Systems).

Fluorescence microscopy. LCLs were spun onto a glass slide at 500 RPM (28*g*) for 1 min in a Shandon Cytospin 4 cytofuge (Thermo Electron). Cells were fixed with 4% paraformaldehyde, permeabilized using 50 μg/ml digitonin and then stained with antibodies to LC3 (clone 1703, Cosmo Bio) and Atg9A[19]. Cells were observed with a confocal laser microscope (FV1000D IX81, Olympus) using a 60× PlanApoN oil immersion lens (1.42 numerical aperture (N.A.), Olympus). For final output, images were processed using Adobe Photoshop 7.0.1 software. The number of staining foci was determined as follows: foci were extracted using the top hat operation (parameter of 300 × 300 pixel area), and a binary image was created. Small foci (with an area of less than 10 × 10 pixels) were removed using an open operation. The number of foci was counted using the integrated morphometry analysis program. False foci were removed by comparison with the original image.

Statistical analysis. Differences were analyzed statistically using unpaired *t* tests or analysis of variance (ANOVA) with a Bonferroni-Dunn post-hoc test.

35. DePristo, M.A. *et al.* A framework for variation discovery and genotyping using next-generation DNA sequencing data. *Nat. Genet.* **43**, 491–498 (2011).
36. Wang, K., Li, M. & Hakonarson, H. ANNOVAR: functional annotation of genetic variants from high-throughput sequencing data. *Nucleic Acids Res.* **38**, e164 (2010).
37. Saitsu, H. *et al. STXBP1* mutations in early infantile epileptic encephalopathy with suppression-burst pattern. *Epilepsia* **51**, 2397–2405 (2010).
38. Kondo, Y. *et al.* A family of oculofaciocardiodental syndrome (OFCD) with a novel *BCOR* mutation and genomic rearrangements involving *NHS*. *J. Hum. Genet.* **57**, 197–201 (2012).
39. Allen, R.C., Zoghbi, H.Y., Moseley, A.B., Rosenblatt, H.M. & Belmont, J.W. Methylation of HpaII and HhaI sites near the polymorphic CAG repeat in the human androgen-receptor gene correlates with X chromosome inactivation. *Am. J. Hum. Genet.* **51**, 1229–1239 (1992).
40. Carrel, L. & Willard, H.F. An assay for X inactivation based on differential methylation at the fragile X locus, *FMR1*. *Am. J. Med. Genet.* **64**, 27–30 (1996).
41. Hosokawa, N., Hara, Y. & Mizushima, N. Generation of cell lines with tetracycline-regulated autophagy and a role for autophagy in controlling cell size. *FEBS Lett.* **580**, 2623–2629 (2006).

A Novel *SCARB2* Mutation Causing Late-Onset Progressive Myoclonus Epilepsy

Progressive myoclonus epilepsy (PME) is a clinically heterogeneous disorder characterized by myoclonus, epilepsy, and progressive neurological deteriorations, typically with cerebellar signs and dementia.[1] Recently, the scavenger receptor class, member 2 gene (*SCARB2*) was found to be mutated in PME with or without renal failure,[2,3] in patients showing preserved intellect, disease onset at approximately 20 years of age, and death usually by 35.[2,4–6] Here, we encountered two Japanese siblings (Fig. 1A) with late-onset PME without renal failure having a novel homozygous *SCARB2* mutation.

Patient 1 (III-9) developed normally. At age 43, myoclonic jerks were noted in her upper limbs when writing. After a few months, gait instability started, leading to falling without loss of consciousness. Action myoclonus and gait instability gradually worsened, and her speech was slurred. She became wheelchair bound at age 51, and bedridden at 54. Now, at 58, cognitive ability, ocular movements, and eyegrounds were preserved (i.e., no cherry-red spots). Generalized hyperhidrosis and dyspnea with marked myoclonus occurred in the stressed condition and/or during anxiety. Tonic clonic seizures also appeared. Biochemical examination indicated healthy renal function. Preserved alpha background activity with no epileptic discharge was found by EEG. Somatosensory-evoked potentials were normal. Brain MRI was normal with no apparent atrophy (Fig. 1B). Brain perfusion single-photon emission computed tomography (SPECT) showed decreased regional cerebral blood flow in the bilateral dorsolateral frontal lobes (Fig. 1C), which might be related to psychiatric symptoms.

The elder brother of patient 1 (patient 2, III-3) developed normally. At age 52, gait instability was noted. At 57, voice and upper-limb tremor triggered by movements was recognized. At 62, he started using a wheelchair and dysphagia occurred. At 63, a convulsive seizure occurred once. At the same age, an acute ischemic stroke on his right corona radiata developed. At 68, regardless of his bedridden state and limb contracture with severe myoclonus triggered by movements, his mental function was preserved. Biochemical examination indicated normal renal function.

To identify the causative mutation, whole exome sequencing was performed using genomic DNA from patient 1. As a result, three homozygous contiguous mutations were detected in exon 11 of *SCARB2*. Sanger sequencing confirmed a homozygous c.1385_1390delinsATGCATGCACC (p.Gly462Aspfs*34) in patient 1, instead of three contiguous mutations (Fig. 1D). The mutation was undetected in 200 Japanese control alleles as well as the public exome database of the National Heart, Lung, and Blood Institute exome sequencing project (5,378 exomes). The mutation cosegregated with those affected (Fig. 1D). To examine whether the frameshift mutation leads to nonsense-mediated messenger RNA (mRNA) decay (NMD), reverse-transcriptase polymerase chain reaction was performed. We confirmed that the amount of mutant *SCARB2* mRNA is comparable to that of wild-type mRNA (Fig. 1E), indicating that mutant mRNA is not subjected to NMD and the abnormal gene product may be postulated. Loss-of-function mutations in *SCARB2* are known to cause PME with or without renal failure.[2,3] Residual SCARB2 function can be related to the exceptionally late-onset PME in these patients.

Legend to the Video

Clinical manifestations of late-onset PME in early and late stages of the disease.

Segment 1: Postural myoclonus and dysdiadochokinesis of patient 1 at 44 years of age.

Supporting Information may be found in the online version of this article.

***Correspondence to:** Dr. Hiroshi Doi, Department of Clinical Neurology and Stroke Medicine, Yokohama City University Graduate School of Medicine, 3-9 Fukuura, Kanazawa-ku, Yokohama 236-0004, Japan; hdoi@yokohama-cu.ac.jp

Funding agencies: This work was supported by a Grant-in-Aid for Young Scientists from the Japan Society for the Promotion of Science (to H.D.).

Relevant conflicts of interest/financial disclosures: Dr. Doi is funded by a Grant-in-Aid for Young Scientists from the Japan Society for the Promotion of Science. Dr. Miyake is funded by research grants from the Ministry of Health, Labor, and Welfare, a Grant-in-Aid for Young Scientists from the Japan Society for the Promotion of Science, and the Takeda Science Foundation. Dr. Saitsu is funded by research grants from the Ministry of Health, Labor, and Welfare, a Grant-in-Aid for Young Scientists from the Japan Society for the Promotion of Science, and Research Grants from the Japan Epilepsy Research Foundation. Dr. Koyano is funded by a Grant-in-Aid for Scientific Research from the Japan Society for the Promotion of Science. Dr. Tanaka is funded by a Grant-in-Aid for Scientific Research from the Japan Society for the Promotion of Science. Dr. Kuroiwa is funded by a Grant-in-Aid for Scientific Research from the Japan Society for the Promotion of Science. Dr. Matsumoto is funded by research grants from the Ministry of Health, Labor, and Welfare and the Japan Science and Technology Agency, the Strategic Research Program for Brain Sciences, a Grant-in-Aid for Scientific Research on Innovative Areas (Transcription cycle) from the Ministry of Education, Culture, Sports, Science, and Technology of Japan, a Grant-in-Aid for Scientific Research from the Japan Society for the Promotion of Science, a Grant for 2011 Strategic Research Promotion of Yokohama City University, and the Takeda Science Foundation.

Full financial disclosures and author roles may be found in the online version of this article.

Received: 18 August 2012; **Revised:** 25 September 2012; **Accepted:** 28 October 2012

Published online 16 January 2013 in Wiley Online Library (wileyonlinelibrary.com). DOI: 10.1002/mds.25296

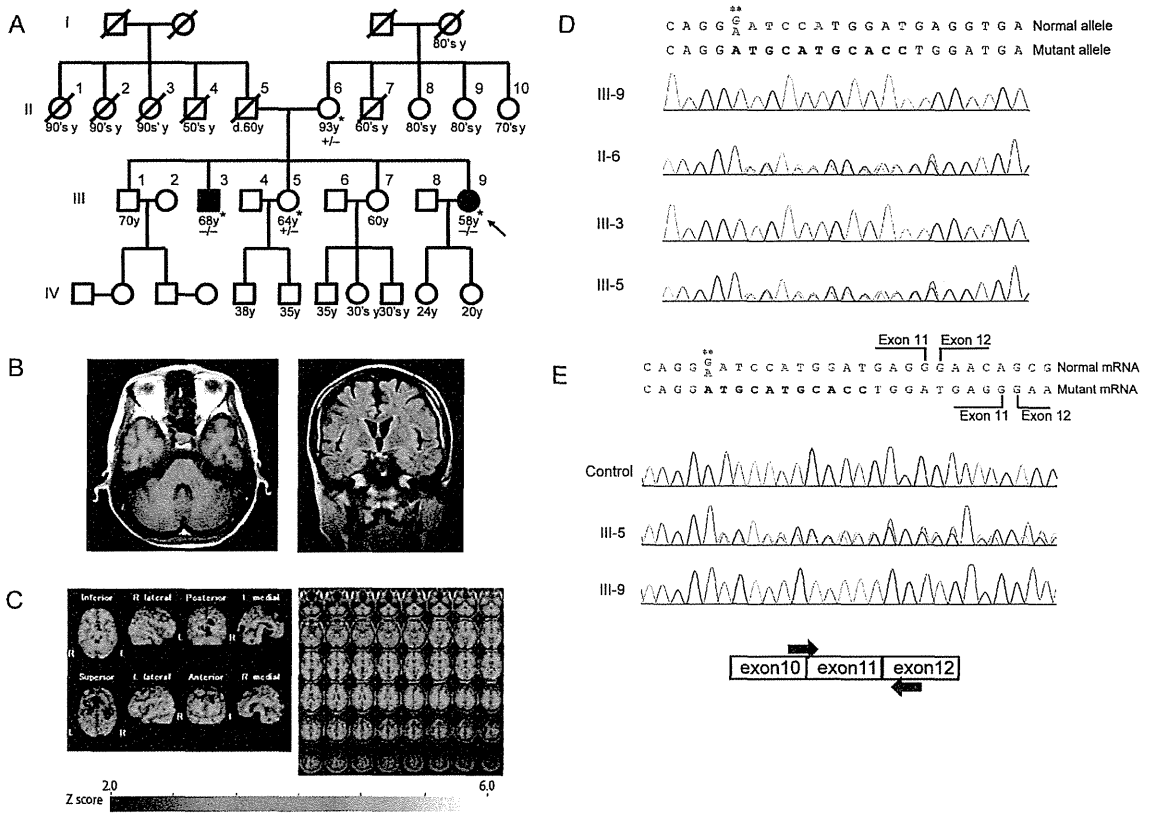

FIG. 1. (**A**) Familial pedigree of cases with PME without renal failure. Individuals with available blood samples are indicated by an asterisk (*). The *SCARB2* mutation is indicated by −/− (homozygous mutation), or +/− (heterozygous mutation). (**B**) MRI findings in patient 1. An axial section of a T1-weighted image (left) and a coronal section of a fluid-attenuated inversion recovery image (right) are shown. No brain atrophy is observed. (**C**) [^{99m}Tc] ethyl cysteinate dimer SPECT in patient 1. To evaluate regional cerebral blood flow, we adopted an easy Z-score imaging system (eZIS).[7] With the eZIS, each SPECT image of the patients was anatomically standardized and compared to the mean and standard deviation (SD) of SPECT images of 30 healthy volunteers 40 to 59 years of age, which had previously been incorporated into the eZIS program as healthy controls. Voxel-by-voxel Z-score analysis was performed after voxel normalization to global mean values: Z-score = (control mean − individual value)/(control SD).[7] (**D**) Electropherogram of the genomic *SCARB2* sequence. The deleted sequence is indicated by gray characters, and the inserted sequence is indicated by bold characters. Heterozygous carriers (II-6 and III-5) in the family have a single-nucleotide polymorphism (rs117157204) on their normal allele (**). (**E**) Electropherogram of *SCARB2* complementary DNA (cDNA). cDNAs from lymphoblasts of a control subject (Control), a heterozygous carrier (III-5), and patient 1 (III-9). Primers used for amplification are indicated by arrows below the electropherogram.

Segment 2: Finger-nose test with action myoclonus of patient 1 at 58 years of age.

Segment 3: Postural myoclonus, dysdiadochokinesis, and action myoclonus of patient 2 at 54 years of age.

Segment 4: Dysdiatochokinesis and finger-nose test with action myoclonus of patient 2 at 68 years of age.

Yuichi Higashiyama, MD,[1] Hiroshi Doi, MD, PhD,[1,2*] Masatoshi Wakabayashi, MD,[3] Yoshinori Tsurusaki, PhD,[2] Noriko Miyake, MD, PhD,[2] Hirotomo Saitsu, MD, PhD,[2] Chihiro Ohba, MD,[1,2] Ryoko Fukai, MD,[1,2] Satoko Miyatake, MD, PhD,[2] Hideto Joki, MD,[1] Shigeru Koyano, MD, PhD,[1] Yume Suzuki, MD, PhD,[1] Fumiaki Tanaka, MD, PhD,[1] Yoshiyuki Kuroiwa, MD, PhD,[1] Naomichi Matsumoto, MD, PhD,[2]

[1]Department of Clinical Neurology and Stroke Medicine, Yokohama City University, Yokohama, Japan; [2]Department of Human Genetics, Yokohama City University, Yokohama, Japan; [3]Ojiya Sakura Hospital, Niigata, Japan

References

1. Classification of progressive myoclonus epilepsies and related disorders. Marseille Consensus Group. Ann Neurol 1990;28:113–116.
2. Berkovic SF, Dibbens LM, Oshlack A, et al. Array-based gene discovery with three unrelated subjects shows SCARB2/LIMP-2 deficiency causes myoclonus epilepsy and glomerulosclerosis. Am J Hum Genet 2008;82:673–684.
3. Dibbens LM, Michelucci R, Gambardella A, et al. *SCARB2* mutations in progressive myoclonus epilepsy (PME) without renal failure. Ann Neurol 2009;66:532–536.
4. Hopfner F, Schormair B, Knauf F, et al. Novel *SCARB2* mutation in action myoclonus-renal failure syndrome and evaluation of SCARB2 mutations in isolated AMRF features. BMC Neurol 2011;11:134.
5. Rubboli G, Franceschetti S, Berkovic SF, et al. Clinical and neurophysiologic features of progressive myoclonus epilepsy without renal failure caused by *SCARB2* mutations. Epilepsia 2011;52:2356–2363.
6. Badhwar A, Berkovic SF, Dowling JP, et al. Action myoclonus-renal failure syndrome: characterization of a unique cerebro-renal disorder. Brain 2004;127:2173–2182.
7. Waragai M, Yamada T, Matsuda H. Evaluation of brain perfusion SPECT using an easy Z-score imaging system (eZIS) as an adjunct to early-diagnosis of neurodegenerative diseases. J Neurol Sci 2007;260:57–64.

ELSEVIER

Brain & Development 36 (2014) 259–263

BRAIN & DEVELOPMENT
Official Journal of the Japanese Society of Child Neurology

www.elsevier.com/locate/braindev

Original article

Different patterns of cerebellar abnormality and hypomyelination between *POLR3A* and *POLR3B* mutations

Jun-ichi Takanashi [a,b,*], Hitoshi Osaka [c], Hirotomo Saitsu [d], Masayuki Sasaki [e], Harushi Mori [f], Hidehiro Shibayama [g], Manabu Tanaka [h], Yoshiko Nomura [i], Yasuo Terao [j], Ken Inoue [k], Naomichi Matsumoto [d], A. James Barkovich [l]

[a] *Department of Pediatrics, Kameda Medical Center, Kamogawa, Japan*
[b] *Department of Radiology, Toho University Sakura Medical Center, Sakura, Japan*
[c] *Division of Neurology, Clinical Research Institute, Kanagawa Children's Medical Center, Yokohama, Japan*
[d] *Department of Human Genetics, Yokohama City University, Graduate School of Medicine, Yokohama, Japan*
[e] *Department of Child Neurology, National Center of Neurology and Psychiatry, Kodaira, Japan*
[f] *Department of Radiology, The University of Tokyo, Tokyo, Japan*
[g] *Department of Neurology, Kameda Medical Center, Kamogawa, Japan*
[h] *Division of Neurology, Saitama Children's Medical Center, Saitama, Japan*
[i] *Segawa Neurological Clinic for Children, Tokyo, Japan*
[j] *Department of Neurology, The University of Tokyo, Tokyo, Japan*
[k] *Department of Mental Retardation and Birth Defect Research, National Center of Neurology and Psychiatry, Kodaira, Japan*
[l] *Department of Radiology and Biomedical Imaging, University of California San Francisco, CA, USA*

Received 21 December 2012; received in revised form 16 March 2013; accepted 27 March 2013

Abstract

Background: Mutations of *POLR3A* and *POLR3B* have been reported to cause several allelic hypomyelinating disorders, including hypomyelination with hypogonadotropic hypogonadism and hypodontia (4H syndrome). *Patients and methods:* To clarify the difference in MRI between the two genotypes, we reviewed MRI in three patients with *POLR3B* mutations, and three with *POLR3A* mutations. *Results:* Though small cerebellar hemispheres and vermis are common MRI findings with both types of mutations, MRI in patients with *POLR3B* mutations revealed smaller cerebellar structures, especially vermis, than those in *POLR3A* mutations. MRI also showed milder hypomyelination in patients with *POLR3B* mutations than those with *POLR3A* mutations, which might explain milder clinical manifestations. *Conclusions:* MRI findings are distinct between patients with *POLR3A* and *3B* mutations, and can provide important clues for the diagnosis, as these patients sometimes have no clinical symptoms suggesting 4H syndrome.

Keywords: Hypomyelination; MRI; Hypomyelination with hypogonadotropic hypogonadism and hypodontia (4H syndrome); Diffuse cerebral hypomyelination with cerebellar atrophy and hypoplasia of the corpus callosum (HCAHC); Cerebellum; *POLR3A*; *POLR3B*; RNA polymerase III (Pol III)

* Corresponding author. Address: Department of Pediatrics, Kameda Medical Center, 929 Higashi-cho, Kamogawa-shi, Chiba 296-8602, Japan. Tel.: +81 470 92 2211; fax: +81 470 99 1198.
E-mail address: jtaka44@hotmail.co.jp (J. Takanashi).

0387-7604/$ - see front matter
http://dx.doi.org/10.1016/j.braindev.2013.03.006

1. Introduction

The term hypomyelination describes a permanent, substantial deficit of myelin deposition in the brain. It is characterized by mild, usually diffuse, hyperintensity of the cerebral white matter on T2-weighted image (T2WI) [1]. Hypomyelinating disorders are numerous, and the growing list of these disorders includes Pelizaeus–Merzbacher disease, Pelizaeus–Merzbacher-like disease, hypomyelination with atrophy of the basal ganglia and cerebellum, and hypomyelination with congenital cataracts. Recently, mutations of *POLR3A* and *POLR3B*, which encode the largest and second largest subunits of RNA polymerase III (Pol III), have been reported to cause allelic Pol III-related hypomyelinating disorders [2–4], including hypomyelination with hypogonadotropic hypogonadism and hypodontia (4H syndrome) [5], leukodystrophy with oligodontia [6], tremor-ataxia with central hypomyelination [7], and diffuse cerebral hypomyelination with cerebellar atrophy and hypoplasia of the corpus callosum (HCAHC) [8]. MRI in patients with clinically diagnosed 4H syndrome revealed cerebellar atrophy in addition to hypomyelination [1]. We noted that, in our patients, the degree of hypomyelination and cerebellar abnormalities seemed to differ between patients with *POLR3A* and *3B* mutations; the latter seemed to have milder hypomyelination and more severe cerebellar abnormality than the former. To substantiate this hypothesis and to define imaging features, we evaluated and compared MRI studies of patients with both mutations.

2. Patients and methods

Three Japanese patients with *POLR3B* and three with *POLR3A* mutations (Table 1) from five hospitals were enrolled in this study. Detailed genetic analysis and a brief summary of the clinical and radiological features of five of the six patients were reported previously [3,9]. MRI data were partly collected through Integrative Brain Imaging Support System at the Integrative Brain Imaging Center, National Center of Neurology and Psychiatry. MRI were performed with 1.5 tesla in three patients, and 3.0 tesla in others. T2WI were obtained using fast spin echo sequences in all patients, while T1WI were scanned with fast spin echo sequences in 4 patients, fast spoiled gradient echo sequence in one patient and fast inversion recovery sequence in another. Two neuroradiologists (JT, HM) reviewed the results of MRI in order to evaluate the state of myelination and the structures of the cerebellum. Myelination was assessed on T1WI and T2WI to look for the degree and extent of T1 and T2 shortening in the cerebral (at the level of the centrum semiovale) and cerebellar white matter, compared with T1WI and T2WI of adult controls, who were evaluated at each hospital for mild neurological symptoms, such as headache or vertigo; scanned with the same sequences as the patients. The cerebellum was assessed for size and degree of enlargement of the fissures in the hemispheres and vermis. It was judged mildly abnormal when the cerebellar hemispheres and vermis were normal in size with mildly thin folia and mildly enlarged fissures, or they are small in size with almost normal folia. A moderately abnormal cerebellum was small with mildly thin folia and mildly enlarged fissures. The cerebellum was severely abnormal when it was small with extremely thin folia and very enlarged fissures.

3. Results

Summaries of the MRI and clinical findings of the six patients are provided in Fig. 1 and Table 1. Three patients with *POLR3B* mutations could walk alone at the age of 16–31, but the two patients with *POLR3A* mutations were wheelchair dependent at ages 7 and 14 years, and another with *POLR3A* mutation needed wheelchair when he walked for a long distance. MRI of the patients with *POLR3B* mutations revealed small cerebellum (hemispheres and vermis) with thin folia and enlarged fissures (judged as moderately abnormal in the hemispheres, and severely abnormal in the vermis). The pattern of decreased cortical thickness and diminished underlying white matter suggested cerebellar atrophy. MRI in the patients with *POLR3A* mutations revealed significantly less severe changes in the cerebellar hemispheres and vermis (judged as mildly to moderately abnormal). The appearance of the vermis, in particular, was distinct between patients with *POLR3B* and *POLR3A* mutations (Fig. 1A–D). Regarding myelination, MRI in patients with *POLR3A* mutations showed high signal intensity on T2WI, and iso to low signal intensity on T1WI, suggesting hypomyelination, in the centrum semiovale (3/3, and 3/3, respectively) and cerebellar white matter (2/3, and 2/3, respectively) (Fig. 1F). In patients with *POLR3B* mutations, T2WI showed high signal intensity of hypomyelination in the centrum semiovale, but normal low signal intensity of myelination in the cerebellar white matter (Fig. 1E). T1WI showed slightly high but lower than normal signal in the centrum semiovale and the cerebellar white matter. Thus, T1WI and T2WI suggest that patients with *POLR3B* mutations had milder hypomyelination than those with *POLR3A* mutations.

4. Discussion

Results of this small series suggest that patients with *POLR3B* mutations have more severe cerebellar abnormalities, but milder hypomyelination, than those with *POLR3A* mutations. The cerebellar hemispheres and vermis were very small, with a pattern suggesting

Table 1
MR imaging findings and clinical features in patients with *POLR3B/3A*.

Pt	Diagnosis	Age/sex	MRI	T2WI						
				TR/TE	CS	PLIC	TH	OR	Cereb WM	DN
1	*POLR3B*	28/M	1.5T	FSE, 4000/90	H	+	–	+	L	–
2	*POLR3B*	31/F	1.5T	FSE, 4000/90	H-I	+	+	+	L	–
3	*POLR3B*	16/F	3T	FSE, 4500/80	H-I	+	+	+	L	+
4	*POLR3A*	15/M	3T	FSE, 5000/80	H	–	+	+	H	+
5	*POLR3A*	17/F	1.5T	FSE, 5286/130	H	–	+	–	H	+
6	*POLR3A*	44/M	3T	FSE, 4400/81	H	+	+	+	L	+

T1W1			Atrophy of cerebellar hemispheres	Atrophy of cerebellar vermis	Sy	Motor level	Ref
TR/TE	CS	Cereb WM					
FSE, 650/10	H	H	Moderate	Severe	G	Able to walk	3 (In-1)
FSE, 650/10	H	H	Moderate	Severe	G	Able to walk	3 (In-2)
FSE, 855/10	H-i	H	Moderate	Severe		Able to walk	3 (In-3)
FIR, 2000/10/858	I-L	I	Mild	Mild		Wheelchair at 14Y	3 (In-4)
FSE, 562/13	I	I	Moderate	Moderate	O	Wheelchair at 7Y	
3D FSPGR, 5.3/1.7	I	H	Mild	Mild	G	Partly wheelchaired	9

Pt, patient; M, male; F, female; T, tesla; T2WI, T2-weigthed image; TR, repetition time; TE, echo time; FSE, fast spin echo; CS, centrum semiovale; PLIC, posterior limb of internal capsule; TH, anterolateral thalamus; OR, optic radiation; Cereb WM, cerebellar white matter; DN, dentate nucleus; T1WI, T1-weighted image; FIR, fast inversion recovery; FSPGR, fast spoiled gradient echo; H, high signal; I, iso signal; L, low signal; +, presence of T2 low signal; –, absence of T2 low signal; Sy, clinical symptoms; G, hypogonadism; O, hypodontia; Ref, reference; In, individual.

cerebellar atrophy, in all six patients with the *POLR3A* and *3B* mutations. As we have no documentation of a normal cerebellum on earlier imaging studies in any of the patients to document that a normal sized cerebellum was ever present, we have chosen to use the term "small" to describe the affected structures. Cerebellar atrophy was found in more than 36 of 40 patients with clinically diagnosed 4H syndrome, often before the age of 10; similar cerebellar findings are uncommon in other hypomyelinating disorders [1]. The present study suggests, in addition, that cerebellar structural abnormality is more severe in patients with *POLR3B* mutations than in those with *POLR3A* mutations. The difference between the two types of mutations was most obvious in the vermis, which was very small in patients with *POLR3B* mutations. MRI in three patients with *POLR3B* mutations reported elsewhere also revealed severely small cerebellar vermis [4], while that in one patient with *POLR3A* mutation showed almost normal vermis and mildly small cerebellar hemispheres [2]; these reports support our observations.

As to myelination, previous studies, showing that T2WI images in three patients with *POLR3B* mutations showed low signal intensity in the cerebellar white matter [4] and that in one patient with *POLR3A* mutation showed high signal intensity [2], support our observations that *POLR3B* mutations have milder hypomyelination. MRI study in clinically diagnosed 4H syndrome showed mild T2 hyperintensity both in the cerebral and cerebellar white matter with a relatively low T2 signal of the optic nerve, the anterolateral part of the thalamus, the posterior limb of the internal capsule, and the dentate nucleus [1], which are compatible with those in patients with *POLR3A* mutation in this study. This may be explained by the fact that *POLR3A* mutation is more common than *POLR3B* mutation as a cause of clinically diagnosed 4H syndrome (19 patients vs. 3 patients) [2,4].

The imaging results of this small study suggest that the MRI pattern of hypomyelination and cerebellar abnormality may be distinct between in patients with *POLR3A* and *3B* mutations. They also suggest that MRI can provide important clues for diagnosing Pol III-related hypomyelinating disorders, especially of *POLR3B* mutations, because patients with *POLR3A* and *3B* mutations do not always have hypogonadism or hypodontia [2,3], which are characteristic of 4H syndrome [5], at the time of presentation, as illustrated by our patients 3 and 4.

Pol III is responsible for the transcription of small noncoding RNAs, such as 5S rRNA, U6 small nuclear RNA, 7SL RNA, RNase P, RNase MRP, microRNA, and all tRNA that might modulate the development of nervous system [10,11]. Dysfunction of Pol III could,

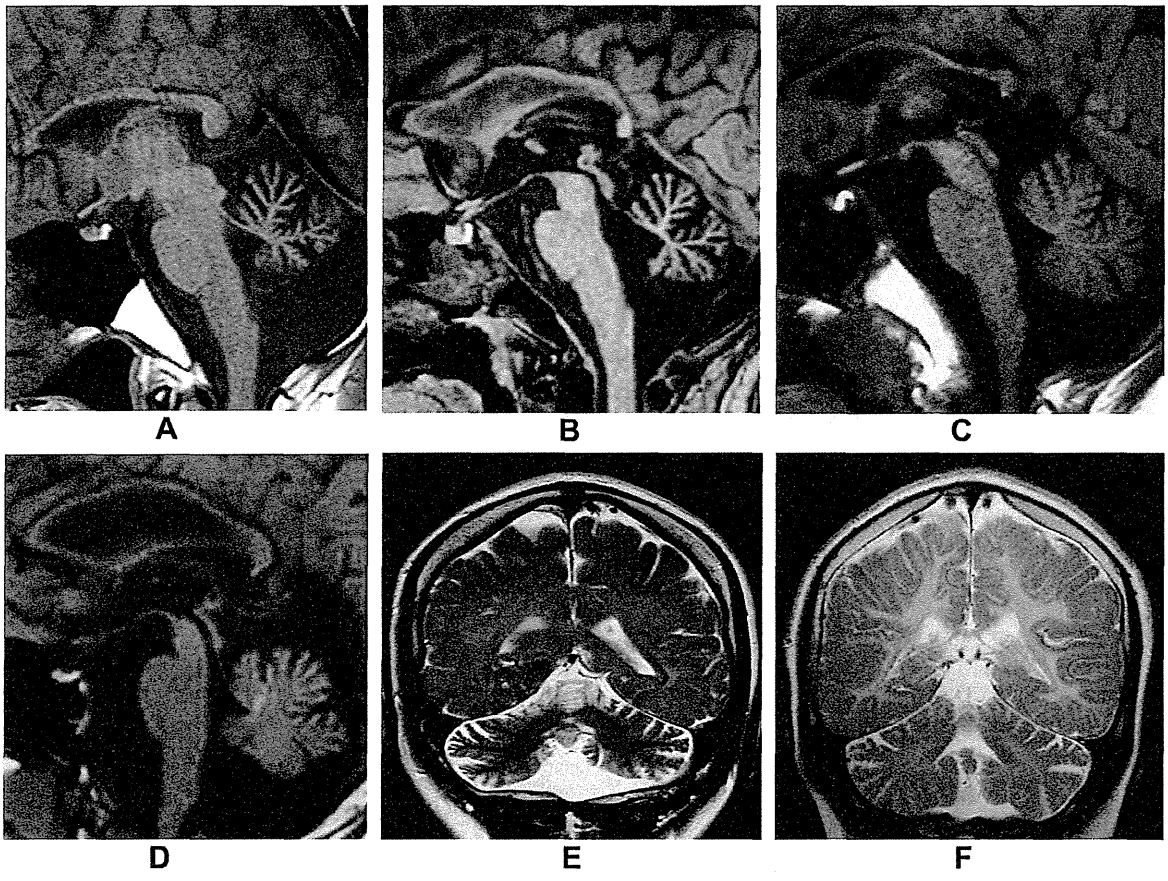

Fig. 1. Sagittal T1WI of patients 1 and 3 (A and B) with *POLR3B* mutations showed very thin vermian folia and enlarged fissures compared with those of patients 4 and 5 (C and D) with *POLR3A* mutations. The appearance suggests atrophy. (C was reused from reference 3 with permission of Elsevier.) Coronal T2WI of patient 1 with a *POLR3B* mutation (E) revealed high signal intensity suggesting hypomyelination in the cerebral white matter and low signal intensity suggesting presence of myelin in the cerebellar white matter. The cerebellar hemispheres appeared moderately small. In contrast, T2WI of patient 4 with a *POLR3A* mutation (F) revealed high signal intensity suggesting hypomyelination in both cerebral and cerebellar white matter, with mildly small cerebellar hemispheres.

therefore, impair the function of certain RNAs that are essential for development and maintenance of myelination, resulting in hypomyelination. Impaired function of tRNAs has also been suggested as pathomechanism in other disorders with white matter involvement (mutations of *DARS2* encoding mitochondrial aspartyl-tRNA synthetase leading to leukoencephalopathy with brain stem and spinal cord involvement and lactate elevation [LBSL]) [12], and cerebellar hypoplasia (mutations of *RARS2* encoding mitochondrial arginyl-tRNA synthetase leading to pontocerebellar hypoplasia type 6) [13]. As POLR3B together with *POLR3A* form the catalytic center of Pol III [14], it is reasonable to postulate that mutations of *POLR3A* and *POLR3B* cause overlapping Pol III-related hypomyelinating syndromes, including the 4H syndrome. Though the cerebellar abnormalities appeared more severe on MRI in patients with *POLR3B* mutations in this study, the patients with *POLR3B* mutations did not have more severe clinical examinations, including cerebellar signs, than ones with *POLR3A* mutations. Patients with both *POLR3A* and *POLR3B* mutations presented with intellectual disability and cerebellar signs, and some had additional clinical symptoms of hypodontia or hypogonadism, as described in the literature [2–4]. All three patients with *POLR3B* mutations in this study could walk without support at the age of 16–31 years, although the two with *POLR3A* mutations were not independent walkers at 7 and 14 years. The clinical severity in patients with *POLR3A* mutations is highly variable even in the same family; however, mean age of loss of ambulation is 16.1 years [2]. These suggest, therefore, that patients with *POLR3B* mutations could be more mildly affected and slowly progressive than those with *POLR3A* mutations; this could potentially be related to the milder hypomyelination found by MRI. Possible explanation for these might be that *POLR3A* is more important than *POLR3B* for the Pol III function, including myelination. Speculation aside, further research regarding the specific metabolic pathways in which these proteins function and how these affect myelination and homeostasis of the cerebellar cortex in laboratory models will be necessary to better understand these

processes. In addition, it will be necessary to examine the clinical and radiological features in a greater number of patients, and to correlate these with specific *POLR3A* and *POLR3B* mutations to determine whether our observations are verified in larger populations and to elucidate the reasons for the apparent disconnection between imaging and clinical observations.

In conclusion, MRI findings in patients with *POLR3A* and *3B* mutations appear to be characteristic and distinct, which could be useful in the work-up of affected patients. For now, patients with hypomyelination and early onset of progressive cerebellar ataxia with the appearance of cerebellar atrophy in childhood should best be considered a subgroup of the 4H syndrome, even if neither hypodontia nor hypogonatotropic hypogonadism is not apparent at the time of initial examination.

Acknowledgement

The authors thank Drs. Noriko Sato and Mrs. Akiko Hattori at National Center of Neurology and Psychiatry, Kodaira, Japan, for their clinical supports.

This study was supported in part by a Research Grant for Nervous and Mental Disorders (24-7) and a Grant-in-aid for the Research on Measures for Intractable Diseases (H22-Nanchi-Ippan-132), both from the Ministry of Health, Labor and Welfare of Japan and by a Grant-in-Aid for Scientific Research (C24591790) from Japan Society for the Promotion of Science.

References

[1] Steenweg ME, Vanderver A, Blaser S, Biizzi A, de Koning TJ, Mancini GM, et al. Magnetic resonance imaging pattern recognition in hypomyelinating disorders. Brain 2010;133:2971–82.

[2] Bernard G, Chouery E, Putorti ML, Tétreault M, Takanohashi A, Carosso G, et al. Mutations of POLR3A encoding a catalytic subunit of RNA polymerase Pol III cause a recessive hypomyelinating leukodystrophy. Am J Hum Genet 2011;89:415–23.

[3] Saitsu H, Osaka H, Sasaki M, Takanashi J, Hamada K, Yamashita A, et al. Mutations in POLR3A and POLR3B encoding RNA polymerase III subunits cause an autosomal-recessive hypomyelinating leukoencephalopathy. Am J Hum Genet 2011;89:644–51.

[4] Tétreault M, Choquet K, Orcesi S, Tonduti D, Balottin U, Teichmann M, et al. Recessive mutations in POLR3B, encoding the second largest subunit of Pol III, cause a rare hypomyelinating leukodystrophy. Am J Hum Genet 2011;89:652–5.

[5] Timmons M, Tsokos M, Asab MA, Seminara SB, Zirzow GC, Kaneski CR, et al. Peripheral and central hypomyelination with hypogonadotropic hypogonadism and hypodontia. Neurology 2006;67:2066–9.

[6] Atrouni S, Darazé A, Tamraz J, Cassia A, Caillaud C, Méqarbané A. Leukodystrophy associated with oligodontia in a large inbred family: fortuitous association or new entity? Am J Med Genet A 2003;118A:76–81.

[7] Bernard G, Thiffault I, Tétreault M, Putorti ML, Bouchard I, Sylvain M, et al. Tremor-ataxia with central hypomyelination (TACH) leukodystrophy maps to chromosome 10q22.3-10q23.31. Neurogenetics 2010;11:457–64.

[8] Sasaki M, Takanashi J, Tada H, Sakuma H, Furushima W, Sato N. Diffuse central hypomyelination with cerebellar atrophy and hypoplasia of the corpus callosum. Brain Dev 2009;31:582–7.

[9] Terao Y, Saitsu H, Segawa M, Kondo Y, Sakamoto K, Matsumoto N, et al. Diffuse central hypomyelination presenting as 4H syndrome caused by compound heterozygous mutations in POLR3A encoding the catalytic subunit of polymerase III. J Neurol Sci 2012;320:102–5.

[10] Dumay-Odelot H, Durrieu-Gaillard S, Da Silva D, Roeder RG, Teichmann M. Cell growth- and differentiation-dependent regulation of RNA polymerase III transcription. Cell Cycle 2010;9:3687–99.

[11] Dieci G, Fiorino G, Castelnuovo M, Teichmann M, Pagano A. The expanding RNA polymerase III transcriptome. Trends Genet 2007;23:614–22.

[12] Scheper GC, van der Klok T, van Andel RJ, van Berkel CG, Sissler M, Smet J, et al. Mitochondrial aspartyl-tRNA synthetase deficiency causes leukoencephalopathy with brain stem and spinal cord involvement and lactate elevation. Nat Genet 2007;39:534–9.

[13] Namavar Y, Barth PG, Kasher PR, van Ruissen F, Brockmann K, Bernert G, et al. Clinical, neuroradiological and genetic findings in pontocerebellar hypoplasia. Brain 2011;134:143–56.

[14] Werner M, Thuriaux P, Soutourina J. Structure-function analysis of RNA polymerases I and III. Curr Opin Struct Biol 2009;19:740–5.

ELSEVIER

Brain & Development xxx (2013) xxx–xxx

BRAIN & DEVELOPMENT
Official Journal of the Japanese Society of Child Neurology

www.elsevier.com/locate/braindev

Case report

RBPJ is disrupted in a case of proximal 4p deletion syndrome with epilepsy

Tojo Nakayama [a,*], Hirotomo Saitsu [b], Wakaba Endo [a,c], Atsuo Kikuchi [a], Mitsugu Uematsu [a], Kazuhiro Haginoya [a,c], Naomi Hino-fukuyo [a], Tomoko Kobayashi [a], Masaki Iwasaki [d], Teiji Tominaga [d], Shigeo Kure [a], Naomichi Matsumoto [b]

[a] *Department of Pediatrics, Tohoku University School of Medicine, Aoba-ku, Sendai, Japan*
[b] *Department of Human Genetics, Yokohama City University Graduate School of Medicine, Kanazawa-ku, Yokohama, Japan*
[c] *Department of Pediatric Neurology, Takuto Rehabilitation Center for Children, Sendai, Japan*
[d] *Department of Neurosurgery, Tohoku University School of Medicine, Aoba-ku, Sendai, Japan*

Received 16 May 2013; received in revised form 13 July 2013; accepted 20 July 2013

Abstract

Proximal 4p deletion syndrome is characterized clinically by mental retardation, minor dysmorphic facial features, and is occasionally complicated with epilepsy. More than 20 cases of proximal 4p deletion syndrome have been reported, but the causative gene(s) remain elusive. We describe here a 2-year-old female patient with a common manifestation of proximal 4p deletion syndrome and infantile epileptic encephalopathy possessing a *de novo* balanced translocation t(4;13)(p15.2;q12.13). The patient was diagnosed as infantile spasms at 9 months of age. She presented with dysmorphic facial features and global developmental delay, compatible with proximal 4p deletion syndrome. Using fluorescence *in situ* hybridization, we determined the translocation breakpoint at 4p15.2 to be within*RBPJ*. RBPJ is a transcription factor in the Notch/RBPJ signaling pathway, playing a crucial role in the developing human brain, and particularly telencephalon development. Our findings, combined with those of previous studies, strongly suggest that *RBPJ* is causative for proximal 4p deletion syndrome and epilepsy in this case.

Keywords: Balanced translocation; Infantile spasms; Proximal 4p deletion syndrome; *RBPJ*

1. Introduction

Deletions involving the proximal portion of human chromosome 4p15 result in a clinically distinct syndrome characterized by variable degrees of intellectual disability, unusual faces, and minor dysmorphic features [1–3]. More than 20 cases of proximal 4p deletion have been reported. The critical region for proximal 4p deletion syndrome has been localized to 4p15.2–15.33, but the causative gene remains elusive.

Infantile spasms (IS), also known as West syndrome, is the most frequent type of epileptogenic encephalopathy. Various types of epileptic spasms, hypsarrhythmia on electroencephalography (EEG), and psychomotor deterioration constitute the basis for a diagnosis of IS. IS is not a nosological entity but rather constitutes a heterogeneous group of conditions that share this clinical triad. Several genetic abnormalities have been identified among the diverse possible causes of IS. Although the number of mutations identified is small, it gives rise to the intriguing possibility that genetic abnormalities underlie a proportion of IS etiology.

* Corresponding author. Address: Department of Pediatrics, Tohoku University School of Medicine, 1-1 Seiryomachi, Aoba-ku, Sendai 980-8574, Japan. Tel.: +81 22 717 7287; fax: +81 22 717 7290.
E-mail address: tojo-nakayama@umin.ac.jp (T. Nakayama).

0387-7604/$ - see front matter © 2013 The Japanese Society of Child Neurology. Published by Elsevier B.V. All rights reserved.
http://dx.doi.org/10.1016/j.braindev.2013.07.009

Here, we present a patient with IS and profound psychomotor delay with a *de novo* reciprocal translocation t(4;13)(p15.2;q12.13) disrupting the gene that encodes recombination signal binding protein for immunoglobulin kappa J (RBPJ).

2. Case report

The patient, a 2-year-old girl, was born after an uneventful pregnancy to unrelated healthy parents at term without asphyxia. Neither parent had intellectual impairment or epilepsy. She experienced clonic convulsions of the extremities at day 20 after birth. An initial EEG performed at 1 month was normal. Her seizures were not well controlled by a combination of phenobarbital and carbamazepine, and gradually evolved into recurrent brief tonic spasms. IS was diagnosed at 9 months of age by intellectual disability, a series of tonic spasms, and modified hypsarrhythmia described as periodic independent polyspikes-wave bursts on EEG.

On examination at 2 years, her weight was 10.7 kg (−0.8 SD) and her height was 86 cm (+0.6 SD). She presented with dysmorphic facial features; upslanted palpebral fissures, epicanthal folds, a large beaked nose, thick lower lips, and micrognathia (Fig. 1a; Table 1). Other minor anomalies included bilateral fifth finger mild brachydactyly (Fig. 1b). A physical examination revealed mild axial hypotonia. She showed global developmental delays with motor skills equivalent to those normally observed at 5 months of age. She was unable to speak any recognizable words. Routine laboratory and neurometabolic investigations, computed tomography scans, and magnetic resonance imaging findings were normal. No abnormalities were seen on an echocardiogram and electrocardiogram. EEG showed diffuse high voltage slow waves with independent spike waves over the bilateral frontal and parieto-occipital area (Fig. 1c and d).

G-banded chromosomal analysis revealed a balanced translocation t(4;13)(p15.2;q12.13) in the patient. Her parents showed a normal karyotype (data not shown), indicating that the translocation occurred *de novo*. Array CGH, according to a method described elsewhere [4] (Supplementary information), did not show any significant copy number variations (data not shown), suggesting that the balanced translocation did not involve occult changes. FISH, performed as previously described [5] (Supplementary information), demonstrated that the putative breakpoint on chromosome 4

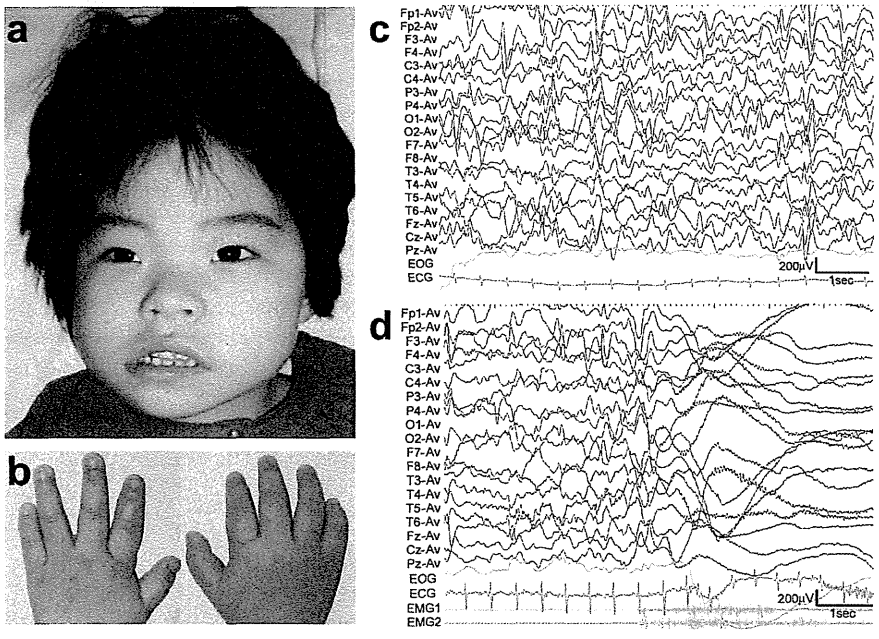

Fig. 1. Characteristics of the patient. (a) Facial appearance of the patient at 4 years. Upslanted palpebral fissures, epicanthal folds, a large beaked nose, thick lower lips, and micrognathia can be observed. Other minor anomalies include strabismus and widely spaced teeth. (b) Digits of the patient at 4 years, showing bilateral fifth finger mild brachydactyly. The parents of the patient gave their consent to publish these photographs in an academic journal. (c) Interictal EEG at 2 years. EEG during wakefulness shows a diffuse high-voltage slow rhythm superimposed with irregular independent spike waves over the bilateral frontal and parieto-occipital area. (d) Ictal EEG during tonic spasms. A diffuse irregular high-voltage slow rhythm is followed by diffuse voltage attenuation with rhythmic fast-wave bursts when tonic axial spasms with symmetric contraction of the deltoid muscles occur. Her daily tonic spasms and subsequent tonic seizures were refractory to pyridoxine, ACTH, valproic acid, clonazepam, lamotrigine, topiramate, and levetiracetam. After undergoing total corpus callosotomy at 2 years and 3 months of age, she showed fewer axial tonic seizures. EOG; electrooculography; ECG; electrocardiography; EMG1; electromyography of left deltoid muscle; EMG2; electromyography of right deltoid muscle.

Please cite this article in press as: Nakayama T et al. *RBPJ* is disrupted in a case of proximal 4p deletion syndrome with epilepsy.. Brain Dev (2013), http://dx.doi.org/10.1016/j.braindev.2013.07.009

Table 1
Clinical features seen in patients with proximal 4p deletion syndrome.

Patient findings	Proband	Francke	Nielsen	Ray	Romain	Fryns	Ishikawa	Davies	White							Chitayat			Van de Graaf	Innes	Tonk		Kojima	Moller	Gawlik-Kuklinska
Publication		1977	1977	1984	1985	1989	1990	1990	1995							1995			1995	1999	2003		2006	2007	2008
									Case 1	Case 2	Case 3	Case 4	Case 5	Case 6	Case 7	Case 1	Case 2	Case 3			Case 1	Case 2			
Breakpoint	p15.2	p11–p15.2	p12–p15	p12–p15	p15.2–p15.33	p14–p15.3	p15.2–p15.32	p15.2–p16.1	p14–p16.1	p15.2–p16.1	p15.1–p16.1	p15.1–p16.1	p15.1–p16.1	p15.1–p16.1	p14–p15.32	p15.2–p15.33	p14–p15.2	p15.2–p15.32	p12–p15.1	p15.2–p16.1	p15.2–p16.1	p15.2–p16.1	p15.2–p15.3	p15.1–p15.3	p14–p15.3
Sex	F	F	F	F	F	M	M	M	M	F	M	F	M	F	F	M	M	F	F	F	F	F	M	F	M
Age	2 years	30 years	12 years	17 years	32 years	12 months	1 month	15.6 years	10 months	nb	19.5 years	37.5 years	33 years	69 years	20 months	10 years	25 years	11 years	7 years	3 years	n/r	6.6 years	16 years	36 years	4 years
Long face	–	+	–	–	–	+	–	–	+	+		+	+	+	–	+	+	+	+	–	+	+	+	–	+
Upslanted palpebral fissures	+	–	n/r	+	–	+	–	–	+	+	+	+	+	+	+	n/r	n/r	n/r	+	–	+	+	n/r	–	+
Epicanthal folds	+	–	+	+	–	+	–	–	+	+	+	+	+	+	+	+	+	–	+	–	+	+	+	–	+
Large beaked nose	+	+	+	+	–	–	–	–	+	–	+	+	+	+	–	–	–	–	–	–	+	+	n/r	–	+
High or cleft palate	–	+	–	–	–	–	+	–	+	+	+	+	+	+	–	+	+	–	–	–	+	–	n/r	–	+
Thick lower lip	+	–	n/r	+	+	+	+	–	+	+	+	+	+	+	+	+	–	+	–	+	+	+	n/r	+	+
Micrognathia	+	–	+	+	–	+	+	–	+	+	+	+	+	–	–	+	+	+	–	–	–	–	+	–	+
Broad short neck	+	+	–	–	–	–	n/r	–	+	+	–	–	n/r	+	+	n/r	n/r	n/r	–	–	–	–	n/r	–	+
Broad hands and feet	–	+	–	+	–	–	n/r	+	+	+	+	+	+	+	–	+	+	–	–	+	–	–	n/r	–	+
Tall, thin habitus	–	+	+	+	+	+	–	+	+	+	+	+	+	+	+	–	–	+	+	–	+	+	–	–	+
Epilepsy	+	–	–	–	–	–	–	–	+	–	–	+	–	–	–	–	–	–	–	–	–	–	+	+	+
Mental retardation	Sev.	Mod.	Sev.	Mod.	Mild	Mod.	Mild	Mod.	Sev.	Sev.	Mod.	Mod.	Mod.	Mod.	Mod.	Mod.	Mod.	Mod.	Mild	Mild	Mild	Mild	Mod.	Mild	Mod.
Neuro image abnormality	–	n/r	n/r	n/r	n/r	n/r	n/r	n/r	n/r	n/r	n/r	n/r	n/r	n/r	n/r	n/r	+[a]	n/r	n/r	n/r	n/r	n/r	n/r	+[b]	+[c]

Studies are listed by the name of the first author. M: male; F: female; n/r: not reported; y: years; mo: months; nb: newborn; +: present; –: absent; Sev.: severe; Mod.: moderate.

[a] Mild brain atropy.

[b] Polymicrogyria of left temproal lobe, left temporal arachnoid cyst.

[c] Periventricular nodular heterotopia.

was located within the *RBPJ* gene (Fig. 2a and b; Supplementary Fig. 1). The breakpoint on chromosome 13 resided in the intergenic region between *GPR12* and *USP12* (Fig. 2c and d). Thus, the balanced translocation in this patient disrupted only one gene, *RBPJ*; this is assumed to lead to hemizygous *RBPJ* loss.

3. Discussion

Proximal 4p deletion syndrome is characterized by a long face, upslanted palpebral fissures, epicanthal folds, a thick lower lip, micrognathia, a large beaked nose, a tall and thin body habitus, broad hands and feet, and varying degrees of mental retardation. There are so far 15 reports describing a total of 24 individuals with deletions involving the proximal portion of human chromosome 4p15 (see Table 1 for details) [1–3, 6–17]. Our patient shares a number of cardinal manifestations of proximal 4p deletion syndrome. The critical region for all of those features has been suggested to be 4p15.2–p15.33 [3]. The disrupted *RBPJ* gene at 4p15.2 in this patient clearly implicates *RBPJ* as a causative gene for proximal 4p deletion syndrome.

Our patient also demonstrated IS followed by intractable childhood epilepsy, with no obvious brain MRI abnormality. The prevalence of epilepsy in cases with proximal 4p deletion is approximately 20%, which is higher than the prevalence rate of epilepsy in general population. The clinical manifestations of previous reported cases are heterogeneous; the seizure types associated with these deletions have been described for five cases, including focal, generalized tonic clonic seizures, and complex partial seizures [2,13–15]. Cerebral abnormalities, such as periventricular heterotopias, polymicrogiria, and arachnoid cyst have been reported in some of these patients with epilepsy [14,15]. While these cerebral abnormalities may account for the presence of epilepsy, the current patient exhibiting epilepsy show no distinctive abnormality in neuro images, which is common for proximal deletion of 4p. Our present case supports the notion that proximal deletion of 4p could lead to variable epileptic phenotypes.

RBPJ is a transcription factor in the Notch/RBPJ signaling pathway. The role of Notch signaling in neuronal development has been intensively analyzed by conditional inactivation of Rbpj in mice; this has revealed that Notch signaling is required for the maintenance of neuronal stem cells [18]. Inactivation of Rbpj induces complete loss of neural stem cells in the developing and adult telencephalon, revealing that RBPJ is likely to play a crucial role in the developing human brain, and particularly telencephalon development [19]. Although we could not confirm the exact pathological role of *RBPJ* abnormalities in epileptogenicity, *RBPJ* haploinsufficiency might increase susceptibility to particular types of epilepsy including IS. Further studies of similar cyto-

Please cite this article in press as: Nakayama T et al. *RBPJ* is disrupted in a case of proximal 4p deletion syndrome with epilepsy.. Brain Dev (2013), http://dx.doi.org/10.1016/j.braindev.2013.07.009

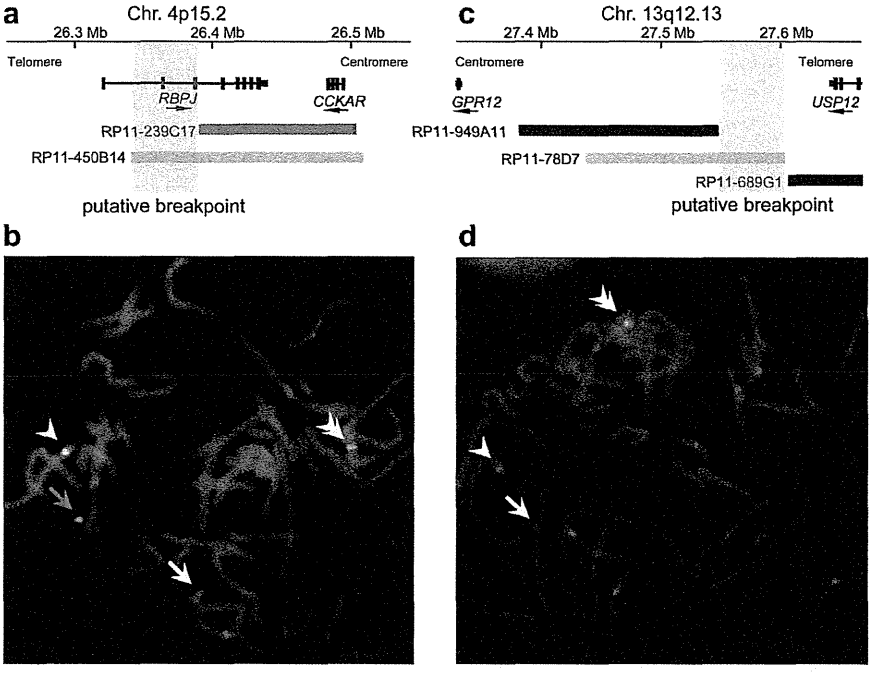

Fig. 2. Characterization of breakpoints by FISH. (a) Schematic presentation of bacterial artificial chromosome probes at the 4p15.2 breakpoint, based on the National Center for Biotechnology Information build 37. Both RP11-239C17 and RP11-450B14 contain *RBPJ* exons. The tan-shaded portion indicates the putative breakpoint region. Horizontal arrows indicate gene orientation. (b) FISH on the patient's chromosomes using RP11-239C17 (red) and RP11-450B14 (green) counterstained with 4′,6-diamidino-2-phenylindole (DAPI) (light blue). Merged signals for RP11-239C17 and RP11-450B14 are seen on the normal chromosome 4 (arrowhead) and the der(4) (double arrowhead); an additional weak signal for RP11-450B14 is detected on the der(13) (arrow), indicating that the *RBPJ* coding region was disrupted by the breakpoint. An artifactual green signal is indicated by the dark gray arrow. (c) Schematic presentation of bacterial artificial chromosome probes at the 13q12.13 breakpoint. Note that RP11-78D7 does not contain any known genes. The tan-shaded box indicates the putative 13q breakpoint region. (d) FISH using RP11-88J11 (red; located at 27.0 Mb on chr. 13; not illustrated in c) and RP11-78D7 (green), counterstained with DAPI (light blue). Merged signals for RP11-88J11 and RP11-78D7 are observed on the normal chromosome 13 (arrowhead) and the der(13) (double arrowhead); an additional weak signal for RP11-78D7 is detected on the der(4) (arrow), indicating that the putative breakpoint (tan-shaded box) is located between the telomeric ends of RP11-949A11 and RP11-78D7. (For interpretation of the references to colour in this figure legend, the reader is referred to the web version of this book.)

genetically proven cases are needed for a better understanding of the pathogenesis of proximal 4p deletion syndrome with epilepsy.

A recent study identified *RBPJ* missense mutations in two families affected by Adams-Oliver syndrome (AOS) [20]; a rare multiple-malformation disorder consisting primarily of congenital cutis aplasia of the scalp vertex, transverse terminal limb defects, and congenital heart defects. Although our current case with hemizygous *RBPJ* disruption presented with bilateral fifth finger brachydactyly, which might be a milder form of terminal limb malformation, no other clinical symptoms were suggestive of AOS. The absence of typical AOS manifestations in our current patient is consistent with previous reports that the phenotypes of patients with proximal 4p deletion syndrome are clinically distinctive from those of AOS. Importantly, proximal 4p deletion syndromes involve at least hemizygous deletion of *RBPJ*, supporting the notion that RBPJ haploinsufficiency is associated with proximal 4p deletion syndrome. Accordingly, our current observations shed light on an aspect of RBPJ function in the central nervous system. Further study of RBPJ aberrations will be required to establish it in a causative role in proximal 4p deletion syndrome as well as epileptic syndromes.

Acknowledgment

This work was supported by a research grant from the Ministry of Health, Labor, and Welfare, Japan (H.S., N.M.), a Grant-in-Aid for Scientific Research from the Japan Society for the Promotion of Science (H.S., N.M.), a research grant from the Japan Science and Technology Agency (N.M.), and the Strategic Research Program for Brain Sciences (a Grant-in-Aid for Scientific Research on Innovative Areas, Foundation of Synapse and Neurocircuit Pathology; N.M.).

Appendix A. Supplementary data

Supplementary data associated with this article can be found, in the online version, at http://dx.doi.org/10.1016/j.braindev.2013.07.009.

Please cite this article in press as: Nakayama T et al. *RBPJ* is disrupted in a case of proximal 4p deletion syndrome with epilepsy.. Brain Dev (2013), http://dx.doi.org/10.1016/j.braindev.2013.07.009